

# High-resolution estimates of Nubia–North America plate motion: 20 Ma to present

S. Merkouriev<sup>1</sup> and C. DeMets<sup>2</sup>

<sup>1</sup>*Pushkov Institute of Terrestrial Magnetism of the Russian Academy of Sciences, St Petersburg Filial. 1 Mendeleevskaya Liniya, St Petersburg, 199034, Russia. E-mail: sam\_hg@hotmail.com*

<sup>2</sup>*Department of Geoscience, University of Wisconsin-Madison, Madison, WI 53706, USA*

Accepted 2013 November 11. Received 2013 November 10; in original form 2013 September 9

## SUMMARY

We present new, detailed estimates of Nubia–North America plate motion since 20 Ma based on 21 rotations that reconstruct seafloor spreading magnetic lineations and fracture zone flow lines between the two plates and an instantaneous angular velocity that best fits the velocities of 1343 GPS stations on the two plates. Total opening distances and opening gradients along the plate boundary are constrained by nearly 11 000 crossings of magnetic reversals 1n (0.78 Ma) to 6n (19.7 Ma) from shipboard and aeromagnetic data surveys of the Mid-Atlantic Ridge between the Azores triple junction and Fifteen–Twenty fracture zone. Plate slip directions are estimated from flow lines digitized from multibeam, single-beam and satellite-based bathymetry for the Oceanographer, Hayes and Atlantis fracture zones. Linear extrapolations of seafloor spreading distances for young magnetic reversals to zero seafloor age shows that magnetic reversal boundaries everywhere along the plate boundary are shifted outwards by  $1 \pm 0.5$  km from the spreading axis with respect to their idealized locations; small corrections to the finite opening rotations to compensate for this outward displacement are thus made to reveal the underlying plate motion. A single inversion of the nearly 13 000 kinematic data is used to estimate the 21 rotations that simultaneously optimize the fits to the reconstructed magnetic lineations and the three fracture zone flow lines and their transform fault traces. Uncertainties in the rotations are estimated via bootstrapping. The new rotations indicate that seafloor spreading rates remained steady from 20 to 8.2 Ma, slowed by 25 per cent between 8.2 Ma and 6.2 Ma, and remained steady since 6.2 Ma within the  $\approx 1$  mm yr<sup>-1</sup> resolution of our new rotations. Our kinematic results corroborate a significant change in motion at  $\approx 7$  Ma previously identified by Sloan and Patriat from a dense magnetic survey of young seafloor from 28°N to 29°N. The timing and magnitude of the change in seafloor spreading between Nubia and North America are the same within uncertainties as those for the Eurasia–North America Plate pair (Merkouriev and DeMets), raising the interesting geodynamic question of why the two should be so similar.

**Key words:** Plate motions; Atlantic Ocean.

## 1 INTRODUCTION

A complete understanding of the Cenozoic history of the Northern Hemisphere, including its palaeogeography, tectonics, palaeoclimate and geodynamics, depends in part on accurate reconstructions of the positions and movements of the hemisphere's largest land masses. In particular, reconstructions of the positions and motions of Eurasia and North America relative to other major plates depend in part on accurate estimates of the relative movement between the North America and Nubia plates across the Mid-Atlantic Ridge between the Azores triple junction and Fifteen–Twenty fracture zone (Fig. 1). Numerous authors have used the seafloor spreading magnetic lineations and fracture zones along this section of the ridge to estimate Nubia–North America finite rotations at  $\approx 5$ –10 Myr inter-

vals from the present back to the opening of the north Atlantic at  $\approx 180$  Ma (e.g. Klitgord & Schouten 1986; Sloan & Patriat 1992; Muller *et al.* 1999; McQuarrie *et al.* 2003).

Most studies of Nubia–North America motion during the Neogene era (23 Ma to the present), the time period of interest in this study, reconstruct Chron 2A ( $\approx 3$  Ma), Chron 5 (10–11 Ma) and Chron 6 (19–20 Ma), which are well surveyed and easily identified in much of the north Atlantic. Unfortunately, the 7- to 8-Myr-long gaps between these reconstructions are too long to detect and date any significant changes in plate motion during the Neogene. The only study to date of Nubia–North America motion at a higher temporal resolution, that of Sloan & Patriat (1992), reports evidence for a simultaneous change in spreading rate, spreading direction, and axial orientation at 7 Ma along a densely surveyed segment of the

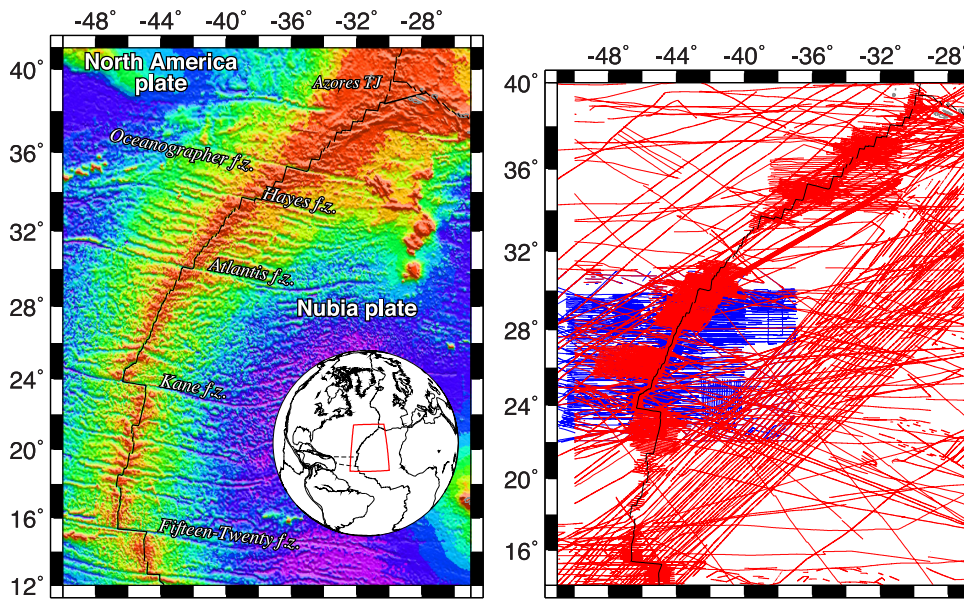


**Figure 1.** Left-hand panel: Location map for study area, with major fracture zones labelled. Red box in the inset map outlines the region shown by the larger map. Right-hand panel: Ship and airplane tracks with magnetic anomaly data used for this study. Blue lines show tracks of Russian surveys from the Bahama–Canary transect (Maschenkov & Pogrebitsky 1992). Red lines show tracks from other sources described in the text. Black line shows axis of the Mid-Atlantic Ridge.

Mid-Atlantic Ridge from 28°N to 29°N. Whether this change was a local kinematic adjustment or is instead evidence for a boundary-wide change in Nubia–North America motion at 7 Ma is unknown. Evidence for a significant change in Eurasia–North America plate motion at  $7 \pm 1$  Ma (Merkouriev & DeMets 2008) raises the possibility of a significant change in plate motion at  $\approx 7$  Ma throughout the north Atlantic and Arctic basins. The potential implications of such a change for our understanding of Neogene era global plate motions, including the recent collisional history of India relative to Eurasia (e.g. Molnar & Stock 2009) and the deformation history of the western United States (e.g. Atwater & Molnar 1973; Atwater & Stock 1998; Wilson *et al.* 2005), are the key motivation for this study.

Herein, we use marine magnetic and bathymetric data from seafloor created along the Nubia–North America segment of the Mid-Atlantic Ridge to estimate plate motion rotations for 21 magnetic reversals that span from Chron 6no (19.7 Ma) to Chron 1n (0.78 Ma). We further estimate instantaneous Nubia–North America motion from the velocities of GPS sites located in the interiors of both plates. Following a description of the underlying data, we describe the fitting functions for magnetic reversal crossings, transform faults and fracture zone flow lines that are used to estimate best-fitting plate motion rotations. These fitting functions and the calibration for outward displacement that is embedded in the inversion procedure constitute a novel method for estimating plate rotations that adopts but moves modestly beyond the method described by Shaw & Cande (1990).

Prior to estimating the sequence of best-fitting rotations, we evaluate the underlying scatter in the magnetic reversal crossings, assign realistic data uncertainties based on the scatter and determine the magnitude of outward displacement along the plate boundary. We then describe the sequence of 21 best-fitting plate motion rotations for C1n to C6no from a simultaneous inversion of the  $\approx 13\,000$  kinematic data we extracted from the shipboard and other measurements from our study area and evaluate their implications for the steadiness or lack thereof in Neogene era Nubia–North America

motion. Our analysis also includes an inversion of 1422 newly estimated velocities for GPS sites in the interiors of the Nubia and North America plates, thereby extending our kinematic model to the present and permitting a useful comparison of Nubia–North America plate motion estimated from our newly derived finite rotations and GPS-based angular velocity.

## 2 DATA

### 2.1 Magnetic reversal crossings

Dense shipboard magnetic coverage of seafloor younger than 20 Ma north of 34°N and from 22°N to 32°N (Fig. 1) provides a superb basis for correlating the full sequence of magnetic anomalies out to Chron 6no and determining the palaeo-axial segmentation necessary for reconstructing magnetic lineations across the ridge. Data from the Russian Canary–Bahamas transect (shown as blue tracks in Fig. 1) densely sample the magnetic field between 22.5°N and 30.5°N (Maschenkov & Pogrebitsky 1992) and constitute our most important source of information about seafloor older than 10 Ma. The well-navigated SARA (Sloan & Patriat 1992), FARA-SEADMA (Gente *et al.* 1995), FARA-SIGMA (Detrick *et al.* 1995) and SudAcores (Cannat *et al.* 1999) cruises provide additional dense coverage, primarily for seafloor younger than 10 Ma. A dense magnetic survey from 14°N to 16°N constrains opening at the southern end of the plate boundary (Fujiwara *et al.* 2003). Magnetic data archived at the U.S. National Geophysical Data Center and magnetic profiles from the Kroonvlag project and other Dutch surveys are also used (Collette *et al.* 1984; Roest & Collette 1986).

The magnetic anomalies from all these sources reveal a complete, uninterrupted magnetic reversal sequence out to seafloor ages of at least 20 Ma between 22°N and 31°N, where there are numerous ridge-perpendicular ship tracks (Fig. 1). Our confidence in these correlations is high and results reported later in the paper are always better determined in this region than elsewhere along the plate boundary.

Due to the sparser shipboard coverage and often oblique orientations of the ship tracks at the northern and southern ends of the plate boundary (i.e. south of 22°N and north of ≈34°N), identifying all the magnetic anomalies in these areas was more challenging. We are relatively confident of most of our correlations of Chrons 1n through 4A in these areas, but are less confident of our correlations of the older anomalies. Likely misidentifications of some older anomalies for some spreading segments in these areas degrades the accuracy of our estimates of seafloor spreading rates and directions at the two ends of the plate boundaries for times before ≈10 Ma. Revisions of our correlations in these areas will be required once better data are available.

Using the above data, we systematically identified all ship crossings of 21 magnetic polarity reversals (listed in Table 1 and displayed in Fig. 2) that range in age from 0.781 Ma (C1n) to 19.7 Ma (C6no). The 21 correlation points coincide with either the young or old edge of a magnetic polarity interval (Fig. 2) and are the same as used in our earlier studies (Merkouriev & DeMets 2006; 2008). With one exception, the reversal ages are adopted from the Hilgen *et al.* (2012) astronomically tuned geomagnetic reversal timescale (Table 1).

We initially identified more than 12 000 crossings of these reversals, but discarded or omitted ≈10 per cent of them during the ensuing analysis due to a lack of confidence in a particular reversal correlation or insufficient crossings of a particular palaeospreading segment. Ultimately, we used 10 769 crossings of the 21 magnetic reversals (Fig. 3) to estimate the finite rotations and plate motion ro-

**Table 1.** Data summary.

Magnetic reversal	Age (Ma)	Number of data			WRMS misfits in km		
		Anom	FZ	TF	Anom	FZ	TF
1no	0.781	710	57	310	1.43	0.37	0.27
2ny	1.778	1009	70	–	1.44	0.69	–
2An.1y	2.581	985	63	–	1.59	1.02	–
2An.3o	3.596	830	67	–	1.55	1.17	–
3n.1y	4.187	701	50	–	1.61	1.29	–
3n.4o	5.235	644	65	–	1.63	1.46	–
3An.1y	6.033	541	51	–	1.65	1.17	–
3An.2o	6.733	493	52	–	1.81	1.16	–
4n.1y	7.528	536	61	–	1.73	1.35	–
4n.2o	8.108	518	50	–	1.57	1.27	–
4Ao	9.105	487	94	–	1.78	1.03	–
5n.1y	9.786	455	83	–	2.11	1.34	–
5n.2o	11.056	522	98	–	2.09	1.40	–
5An.2o	12.474	383	148	–	1.90	0.79	–
5ACy	13.739	315	128	–	2.26	0.41	–
5ADo	14.609	295	124	–	2.34	0.69	–
5Cn.1y	15.974	297	131	–	2.07	1.34	–
5Dy	17.235	269	132	–	2.02	2.55	–
5Ey	18.056	245	92	–	1.90	3.21	–
6ny	18.748	255	96	–	2.25	3.94	–
6no	19.722	279	75	–	2.29	4.72	–

Notes: Chron designators followed by a ‘y’ or ‘o’, respectively, indicate the young or old edge of the chron. Reversal ages are from the astronomically tuned Neogene timescale of Hilgen *et al.* (2012), except for Anomaly 4n.1y, which is from Lourens *et al.* (2004). Anom, FZ and TF, respectively, indicate the number of magnetic reversal, fracture zone and transform fault crossings used to estimate the finite rotations listed in subsequent. Ages estimated for the fracture zone crossings are approximated from their distances along their respective flow lines, although in the inversion, every fracture zone crossing contributes information to the finite rotation estimates for each chron. WRMS is the weighted rms misfit in kilometres of the best-fitting rotation adjusted for the number of parameters that were estimated in order to fit the given data subset.

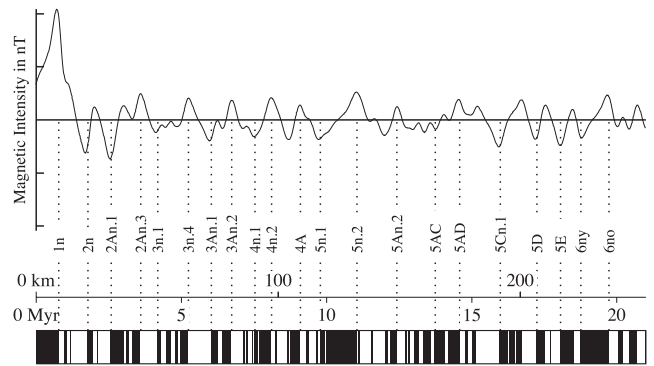


**Figure 2.** Correlation points for the 21 magnetic reversals used to estimate Nubia–North America motion. The synthetic magnetic profile for the anomaly sequence east of the ridge was created using a half spreading rate of 12 km Myr<sup>-1</sup>, an assumed 500-m-wide reversal transition zone, and ambient and palaeomagnetic inclinations and declinations appropriate for the study region. The magnetic block model and 21 correlation points (dotted lines) appear below the synthetic magnetic anomaly profile.

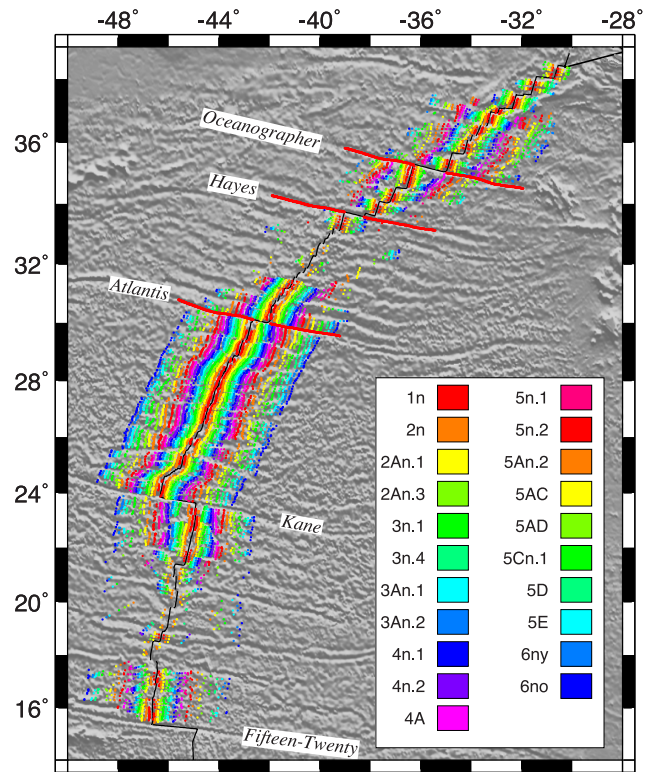


**Figure 3.** Crossings of magnetic reversals 1n through the old edge of Chron 6n identified in Fig. 2 and Table 1, and digitized fracture zone flow lines (red circles). Inversions of these data are the basis for the reconstructions shown in Figs 10–12. Neither the Kane nor the Fifteen-Twenty fracture zones are used to estimate Nubia–North America Plate reconstructions.

tations that constitute the new kinematic model. Table 1 documents the number of crossings used per reversal, ranging from more than 1000 for Chron 2n to ≈250 for some of the more sparsely surveyed, older anomalies. Superb coverage of the magnetic reversal sequence between 22°N and 32°N (Fig. 3) allows us to recover palaeospreading rates, palaeoslip directions and the segmentation of the palaeospreading centre in this region with high confidence.

Reconstructions of the reversal crossings shown in Fig. 3, as well as their dispersions relative to best-fitting models and the influence of outward reversal displacement are presented in a later section.

## 2.2 Fracture zone and transform fault crossings

Following Shaw & Cande (1990), we also use fracture zone flow lines to estimate the sequence of finite rotations that constitute the kinematic model. Four fracture zones offset the Nubia–North America segment of the Mid-Atlantic Ridge, namely, the Oceanographer, Hayes, Atlantis and Kane fracture zones (Fig. 1). For each of these, we used bathymetric grids available through the Marine Geoscience Data System ([www.marine-geo.org](http://www.marine-geo.org) and Carbotte *et al.* 2004) to identify and digitize a continuous flow line on both sides of the ridge, including the transform fault (Fig. 3). We digitized points every 500–1000 m along each fracture zone, thereby approximating the spacing of the multibeam bathymetric or satellite altimetric observations that were used to build the bathymetric grids. The flow line for the Kane fracture zone was identified from complete multi-beam coverage of the fracture zone valley on both sides of the ridge to seafloor ages of 20 Ma. Flow lines for the Hayes and Atlantis fracture zones were based on varying degrees of multibeam and altimetric coverage. The Oceanographer flow line was based entirely on satellite altimetric coverage of the fracture zone and multibeam mapping of the transform fault valley.

For reasons described later, we excluded crossings of the Kane fracture zone and Kane transform fault from our inversion for a best-fitting kinematic model. We did however use the trace of the Kane FZ to test the predictive ability of our new rotations.

The  $1\text{-}\sigma$  uncertainties we assigned to fracture zone crossings varied along-strike depending on the local width of the fracture zone valley. Fracture zone crossings digitized from well-defined lineaments imaged with multibeam were assigned uncertainties as small as 1–2 km. Fracture zone crossings digitized from wide, flat-bottomed segments of fracture zone valleys were assigned uncertainties of 5–10 km depending on the valley width. Prior to the final inversion of our kinematic data, all the fracture zone uncertainties were scaled systematically to balance the information they contributed to the solution with the information contributed by the magnetic reversal crossings. Misfits to these data are described in a later section.

## 2.3 GPS site velocities

Data from 1343 GPS stations located in the interiors of the North America and Nubia plates are used to determine the instantaneous motion between the two plates. These data span the period from early 1996 to June of 2012. Raw GPS were processed with release 6.1 of the GIPSY software suite from the Jet Propulsion Laboratory (JPL). No-fiducial daily GPS station coordinates were estimated using a precise point-positioning strategy (Zumberge *et al.* 1997), including constraints on *a priori* tropospheric hydrostatic and wet delays from Vienna Mapping Function (VMF1) parameters (<http://ggsatm.hg.tuwien.ac.at>), elevation- and azimuthally dependent GPS and satellite antenna phase centre corrections from IGS08 ANTEX files (available via ftp from [sidshow.jpl.nasa.gov](http://sidshow.jpl.nasa.gov)), and corrections for ocean tidal loading (<http://holt.oso.chalmers.se>). Wide- and narrow-lane phase ambiguities were resolved using GIPSY's single-station ambiguity resolution feature.

All daily no-fiducial station location estimates were transformed to IGS08 using daily seven-parameter Helmert transformations

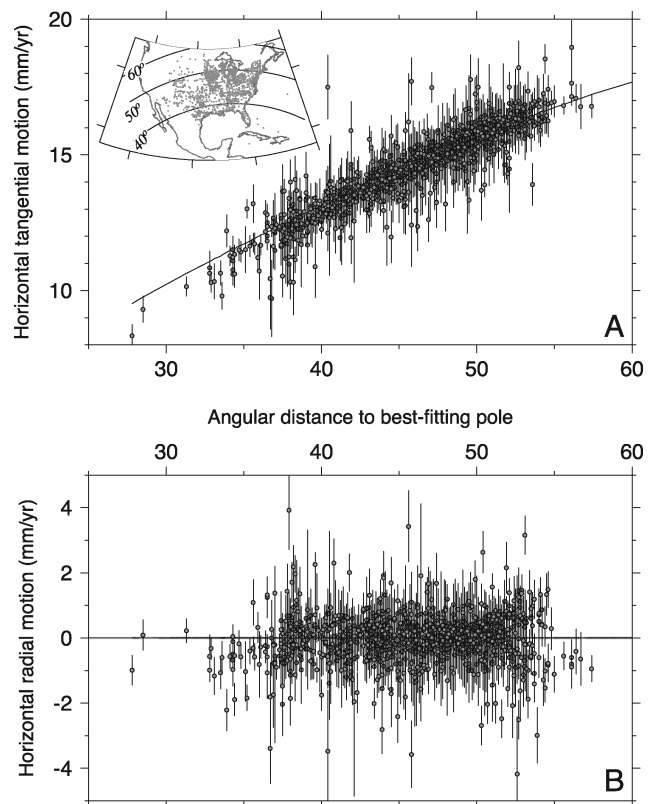


**Figure 4.** Locations (map inset) and velocity components of 1294 North America Plate GPS sites used to estimate the instantaneous North America Plate angular velocity. Geodetic reference frame is ITRF2008. Site locations are indicated by grey circles in the map inset. (A) Component of each station's velocity parallel to a small circle around the best-fitting pole. (B) Component of station motion towards or away from the best-fitting pole (the radial component). Standard errors are shown.

from JPL. Since IGS08 conforms to the widely used ITRF2008 (Altamimi *et al.* 2011), we refer hereafter to ITRF2008 as the underlying geodetic reference frame. We assume that the geocentre as defined in ITRF2008 is stable and make no correction for possible geocentral motion (Argus 2007). Spatially correlated noise between GPS sites is estimated from the coordinate time-series of well-behaved continuous stations from within and outside the study area and is removed from the time-series of all sites (Marquez-Azua & DeMets 2003). After the noise corrections are applied, the day-to-day variations in the northing and easting components of the station coordinates range from 0.6 to 2 mm ( $1\text{-}\sigma$ ).

All 1294 GPS stations that we inverted to determine the North America Plate angular velocity are located east of the Basin and Range province of western North America and south of the US–Canada border (see map inset for Fig. 4). The latter limit was selected to reduce the effect of glacial isostatic rebound, which causes slow but systematic southward motion of GPS stations away from ice sheet depocentres in Canada during the previous ice age (Calais *et al.* 2006; Sella *et al.* 2007). The velocities for the North America Plate GPS sites are well fit by the best-fitting angular velocity (Fig. 4), with 68.3 per cent of the total residual misfits smaller than  $0.6\text{ mm yr}^{-1}$ .

The 49 GPS sites used to estimate the Nubia Plate angular velocity are located west of the East Africa rift (see map inset for Fig. 5). The Nubia site velocities span a large angular distance with respect to their best-fitting pole (Fig. 5) and thus impose strong geometric

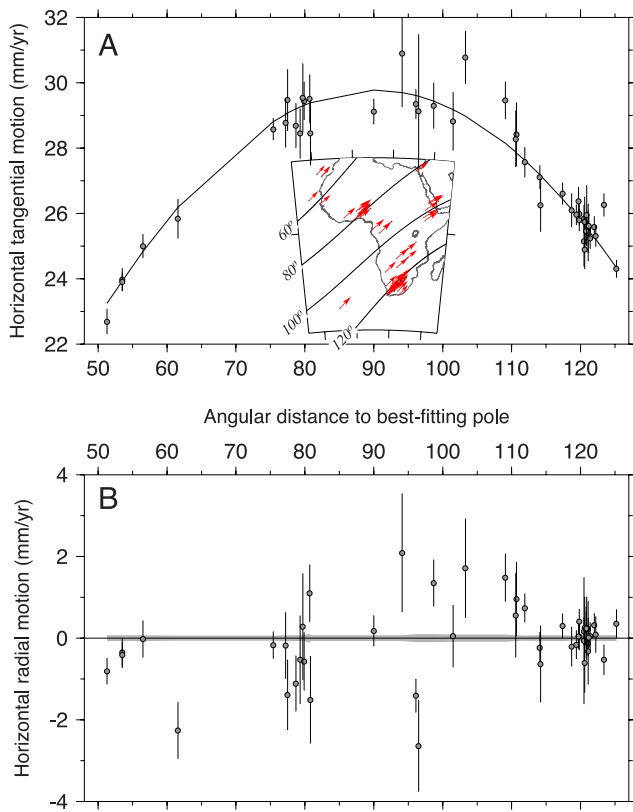


**Figure 5.** Locations (map inset) and velocity components of 49 Nubia Plate GPS sites used to estimate the instantaneous Nubia Plate angular velocity. Red arrows in map inset show GPS site velocities in ITRF2008. (A) Component of each station's velocity parallel to a small circle around the best-fitting pole. (B) Component of station motion towards or away from the best-fitting pole (the radial component). Standard errors are shown.

constraints on both the pole location and angular rotation rate. The uncertainties in many of the Nubia Plate site velocities are larger than  $1 \text{ mm yr}^{-1}$  because many of these sites only began operating in the past few years. Reflecting their larger uncertainties, the rms misfit,  $1.1 \text{ mm yr}^{-1}$ , is twice that of the North America Plate velocity field.

### 3 ANALYSIS TECHNIQUES

#### 3.1 Estimation of plate rotations and uncertainties

The method we use to estimate best-fitting rotations differs in important respects from that we employed previously (Merkouriev & DeMets 2006, 2008). Previously, magnetic reversal and fracture zone crossings were grouped into a series of conjugate spreading and fracture zone segments that define the palaeoplate boundary on opposite sides of a seafloor spreading centre. The observations were then inverted to identify the rotation that best reconstructed the ensemble of spreading and fracture zone segments from one plate onto their conjugate segments on the other plate. The same minimum-distance, great-circle fitting criteria (Hellinger 1979, 1981) was applied to both the magnetic reversal and fracture zone data to find the misfit of the trial rotation.

Here, we use a modified estimation technique that recognizes the inherently different constraints that magnetic reversal, fracture zone and transform fault data impose on plate rotations. The new method preserves the rigorous treatment of magnetic reversal reconstruc-

tions pioneered by Hellinger (1979, 1981) and improved by Chang (1988) and Royer & Chang (1991), but uses separate fitting functions for fracture zone flow lines and transform faults. Data from all the times represented by the data are inverted simultaneously in order to implement the fracture zone flow line fitting function. Details are given later.

The angular velocity that best fits a given set of GPS site velocities is determined via a weighted least-squares inversion that employs fitting functions described by Ward (1990). Formal uncertainties in the angular velocities are specified by a  $3 \times 3$  covariance matrix that is propagated linearly from the uncertainties in the GPS site velocities.

##### 3.1.1 Magnetic reversal fitting criteria

Following previous practice, the crossings of each magnetic reversal are grouped into  $P$  distinct palaeospreading segments that define the palaeospreading centre when they are reconstructed. After reversal crossings from the moving plate are rotated onto the stationary plate, the misfit for each reversal crossing that is affiliated with a reconstructed spreading segment is equated to the minimum distance between the datum and the great circle that best fits the ensemble of reconstructed points that define the segment (Hellinger 1979, 1981). The summed-squared misfit per reconstructed segment is thus the sum of the squared distances divided by the estimated location uncertainties for the reversal crossings that define the segment. In addition to the three rotation parameters that are estimated,  $2 \times P$  parameters that consist of the poles to the best-fitting great-circle segments are estimated to fit magnetic reversal crossings.

##### 3.1.2 Fracture zone flow line fitting criteria

Following Shaw & Cande (1990), we use a flow-line fitting criteria to fit fracture zone flow lines on the moving and stationary plates. The trace of a fracture zone within its valley describes the path travelled by the present ridge–transform intersection. Assuming that the ridge–transform intersection did not propagate along-axis or jump to a different location during the interval of interest, the trace of the fracture zone should be well described by a flow line that originates at its ridge–transform intersection and is reconstructed from a time progression of half-stage rotations that are derived from the finite rotations that best describe the spreading centre's opening history.

To implement fitting of fracture zone flow lines within the framework of our finite rotation estimation method, a sequence of  $N$  trial finite rotations is estimated simultaneously from magnetic reversal crossings for those  $N$  times and from fracture zone flow-line crossings from one or both sides of the ridge. Stage rotations for both the stationary and moving plates are determined from the trial finite rotations for all time-adjacent intervals from the present to the oldest time modelled. Half-stage rotations are then used to reconstruct the path of each ridge–transform intersection on its respective plate, assuming symmetric seafloor spreading. The misfit to each point that defines a fracture zone flow line crossing is defined by its distance to the predicted flow-line path along a great circle locally orthogonal to the observed flow line. Readers are referred to Shaw & Cande (1990) for a more complete description.

##### 3.1.3 Transform fault fitting criteria

Continuous strike-slip faults within transform fault valleys describe small circles (i.e. lines of pure slip) around the youngest pole of

opening and are therefore useful for determining the location of the youngest opening pole. Using the fact that points along a small circle are equidistant from the pole at its centre, we designed a small-circle fitting function for our rotation estimation software as follows: For each transform fault whose trace is represented by two or more digitized points, the angular distance from the youngest trial rotation to each point along the transform fault is determined. The misfit for each point along the transform fault trace is then defined as the difference between that point's angular distance to the opening pole and the mean angular distance for all the points that define the fault segment. One parameter is estimated per transform fault segment, namely, its mean distance to the pole.

We assume that the faults within a transform fault valley reconfigure rapidly to changes in plate motions or local stress conditions. We therefore use transform faults to help locate only the opening pole for Chron 1n (0.78 Ma).

### 3.2 Search algorithm and output

For a single time interval and palaeoplate boundary with  $P$  spreading segments,  $Q$  fracture zone flow lines and  $R$  transform faults (limited to the youngest time interval), the cumulative weighted least-squares misfit  $\chi^2$  for a trial rotation is the sum of the misfits for the three data types. Per time interval, the number of parameters estimated from the data is equal to  $3 + 2P + R$ , consisting of the three rotation parameters,  $2P$  parameters that represent the best-fitting great circles for the  $P$  reconstructed spreading segments and  $R$  mean angular distances from the best-fitting rotation pole to each transform fault. Based on information provided by the user, our software also corrects for systematic shifts in reversal locations due to the effect of outward displacement. This is an important feature for studies of recent plate motions, for which opening rate estimates may be upward-biased by as much as 30 per cent absent any correction for outward displacement.

Data from all the time intervals are inverted simultaneously to determine a best-fitting time progression of finite rotations and hence stage rotations. A downhill simplex technique (Chang 1988) is used to find the sequence of finite rotations, optionally corrected for outward displacement, that minimize the weighted least-squares misfit  $\chi^2$ . A simultaneous inversion of data that consists solely of magnetic reversal crossings from  $T$  time intervals would yield a sequence of  $T$  uncorrelated finite rotations, no different than if the data from each time were inverted separately. In contrast, a simultaneous inversion of magnetic reversal and fracture zone flow line data introduces correlations between the finite rotations for all the times represented by the data (since an adjustment to one finite rotation requires adjustments to all the other finite rotations in order to preserve the sequence of stage rotations that best describes the ensemble of fracture zone flow lines). Care must thus be taken in introducing the flow line data since inaccuracies in one or more flow lines can degrade the estimates of finite rotations for multiple times.

Outputs of the new software include finite rotations for each time, formal rotation covariances based on the geometries of the reconstructed palaeoplate boundary and fracture zone flow lines, the weighted rms misfits for all data types and times included in the inversion and a variety of files necessary for visualizing the reconstructed spreading segments and synthetic flow lines.

In the latter part of the analysis, we use stage rotations and their covariances determined from the best-fitting finite rotations to describe spreading rates, spreading directions and their uncertainties during 2- to 3-Myr-long intervals since 20 Ma. For the 16 magnetic

reversals whose ages are astronomically calibrated, errors in their estimated ages are unlikely to exceed  $\pm 10\,000$  yr (Lourens *et al.* 2004). For comparison, the shortest averaging interval we use to estimate stage spreading rates,  $\approx 1.5$  Myr, is 150 times longer than the interval uncertainty. The implied  $1\sigma$  error in the stage spreading rate is less than 1 per cent or  $\pm 0.1$  to  $0.2$  mm yr<sup>-1</sup> of the 20–25 mm yr<sup>-1</sup> Nubia–North America spreading rates that have prevailed since 20 Ma. This is a factor of 2–10 smaller than the uncertainties propagated from the stage rotation covariances and thus do not represent an important limiting factor in our analysis.

Finally, stage spreading rates are nearly insensitive to the biasing effects of outward displacement because any bias attributable to outward displacement is common to all of the finite rotations and thus cancels when the finite rotations are combined to estimate stage rotations.

### 3.3 Rotation uncertainties from bootstrapping

Following Merkouriev & DeMets (2006), we estimate all the finite rotation uncertainties using a bootstrapping procedure that overcomes two limiting assumptions that are made when estimating rotation covariances from the geometry of a reconstructed plate boundary and the number of data used to estimate a rotation (Chang 1988; Kirkwood *et al.* 1999). The first assumes that uncertainties in the locations of individual magnetic reversal and fracture zone crossings are random and uncorrelated between data. The second assumes that the reversal correlations and identifications of conjugate palaeoridge segments are correct everywhere along the reconstructed plate boundary.

From a Monte Carlo analysis of data from the Carlsberg Ridge, Merkouriev & DeMets (2006) find that the first of these two assumptions is incorrect. They present evidence for systematic shifts of  $\approx 1.6$  km of reversal edges both towards and away from the ridge with respect to their expected locations, roughly 1 km more than expected for reconstructions of reversal crossings with random uncorrelated errors equal to those observed for the Carlsberg Ridge. Systematic shifts of many or all the reversal crossings from a given spreading segment away from the expected reversal location might result from anomalous skewness (Roest *et al.* 1992), changes in the width of the magnetic reversal polarity transition zone along the ridge (DeMets and Wilson 2008) and incorrectly identified conjugate palaeoridge segments. Rotation covariances that ignore the segment-specific systematic errors may understate the true rotation uncertainties by a factor of two or more (Merkouriev & DeMets 2006).

Misidentifications of one or more magnetic reversals in a reversal sequence are also a potential source of correlated errors for nearby reversal crossings. This is less of a concern for well-mapped segments with uninterrupted reversal sequences (e.g. 24–32°N) than for sparsely mapped regions or regions with low-fidelity anomalies (e.g. 18–22°N).

To overcome these, we use the bootstrapping procedure described by Merkouriev & DeMets (2006). As implemented herein, the segment-based bootstrap method works as follows: We created 1500 randomized data samples selected from the  $P$  palaeospreading segments,  $Q$  fracture zone flow lines and  $T$  transform faults available for the Nubia–North America Plate boundary. For each of the 21 magnetic reversals, we randomly selected  $P$  segments from all the available segments and added those to the data sample, such that all the reversal crossings from  $21 \times P$  randomly selected spreading segments are included in each data sample. Similarly,  $Q$  fracture

zones and  $T$  transform faults were also selected randomly from those available and added to the data sample. Each randomized data sample thus includes the same number of spreading segments, fracture zones and transform faults as the original data sample. The randomized samples however capture a wider range of possible segment combinations and relative segment weights than is the case for the original population of data.

Due to its random nature, the above procedure may omit particular spreading segments, fracture zones or transform faults from some data samples, or include them multiple times in others. The effects of any segment-specific errors caused by systematic misidentifications of a particular magnetic reversal, an imprecisely interpreted fracture zone flow line or transform fault strand, or a variety of other systematic errors that can influence the location of a particular magnetic reversal for a spreading segment are thus well explored via bootstrap data sampling. Uncertainties estimated via this procedure constitute more conservative estimates of the likely uncertainties in the rotation parameters than the formal rotation covariances, which presume that the underlying data errors are random.

All best-fitting rotations described later in the analysis are the average of the rotations derived from inversions of the bootstrapped data samples described earlier. The rotation covariances are derived from the  $3 \times 3$  orientation matrix (Fisher *et al.* 1993) for the ensemble of the bootstrapped rotations.

### 3.4 Characterization of data misfits

Following Royer & Chang (1991), we use  $\hat{k} = (N - m) / \chi^2$  as a measure of the dispersion of the observations with respect to the predictions of our best-fitting rotations, where  $N$  is the number of observations,  $m$  is the number of parameters that are used to fit the data and  $\chi^2$  is the weighted least-squares misfit to the data. Since the number of data is large for all three of our data types,  $\hat{k}$  for the individual data types is well approximated by  $(N_{\text{mag}} - 2P) / \chi^2_P$  for  $N_{\text{mag}}$  magnetic reversal crossings grouped into  $P$  segments,  $(N_{\text{tf}} - R) / \chi^2_R$  for  $N_{\text{tf}}$  transform fault crossings of  $R$  transform faults and  $N_{\text{fz}} / \chi^2_Q$  for  $N_{\text{fz}}$  fracture zone flow line crossings of  $Q$  flow lines.

Values of  $\hat{k} \approx 1$  indicate that the data uncertainties are approximately correct, whereas values of  $\hat{k}$  that are significantly greater or less than 1 indicate that the uncertainties are, respectively, overestimated or underestimated by a factor of  $\sqrt{\hat{k}}$ . The dispersions of each type of data are used to rescale their originally assigned uncertainties such that  $\hat{k} \approx 1$  for each data type in the final inversion. Further information about these misfits is given later.

Merkouriev & DeMets (2006) demonstrate that uncertainties in magnetic reversal crossings include random errors and two sources of systematic error. One source of systematic error is outward displacement, defined as the displacement of magnetic reversal boundaries away from the axis of seafloor spreading due to the finite-width zone across which new seafloor accretes and records magnetic polarity transitions (e.g. Sempere *et al.* 1987). *In situ* studies of seafloor magnetic polarity transitions indicate that reversal boundaries are displaced outwards by 1–5 km with respect to their idealized locations (e.g. Macdonald *et al.* 1983; Sempere *et al.* 1987). Detailed kinematic studies of young seafloor spreading lineations independently confirm both the widespread occurrence of outward displacement and the 1–5 km magnitudes measured *in situ* (Merkouriev & DeMets 2006, 2008; DeMets & Wilson 2008).

Correcting for outward displacement of reversal boundaries is critical for estimates of young rotations, particularly at slow spreading rates. For example, at a  $20 \text{ mm yr}^{-1}$  full spreading rate, only

15.6 km of seafloor has accreted since Chron 1n (0.78 Myr). Assumed outward displacement of 1 km on each side of the ridge widens Anomaly 1n by 2 km (13 per cent), thereby yielding an apparent recent acceleration in seafloor spreading. Outward displacement also alters the apparent opening gradient along the plate boundary, resulting in biased estimates of opening pole locations.

The second source of systematic error, referred to hereafter as segment-specific systematic error, is described in the previous section and is accounted for via a data bootstrapping procedure described in the previous section.

### 3.5 Validation with synthetic plate boundary data

We tested the data fitting functions and downhill simplex search algorithm described earlier by inverting noisy synthetic data constructed from a known sequence of rotations, as follows: For a hypothetical plate boundary defined by six spreading segments, five transform faults and five fracture zones (Fig. 6), we use a time sequence of four finite rotations with different poles and opening angles to populate each plate boundary element with synthetic data. Transform faults were required to describe small circles around

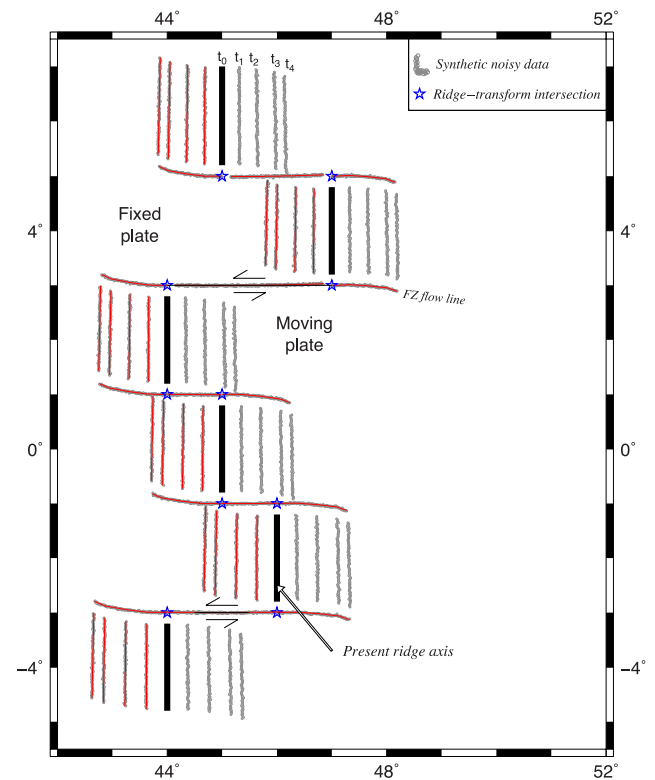


**Figure 6.** Test of inversion method and fitting functions with synthetic, noisy data from a hypothetical plate boundary with six spreading segments, five transform faults and five fracture zone flow lines per fixed and moving plate. Synthetic magnetic reversals for times  $t_1$  to  $t_4$  are constructed on both sides of each spreading segment for a time progression of four known rotations. Synthetic transform faults between the ridge–transform intersections follow small circles around the youngest rotation pole. Synthetic fracture zone flow lines are created from stage rotations determined from the finite rotations. An inversion of the noisy synthetic data successfully recovers the starting rotations and fits the data well. Red lines show the reconstructed palaeospreading segments (great circles), transform faults (small circles) and fracture zone flow lines for the sequence of finite rotations that best fit the data. The fits are visually indistinguishable from the reconstructed data for all three data types.

the youngest pole; fracture zone flow lines that begin at the ends of the transform faults followed the path dictated by half-angle stage rotations determined from the four finite rotations; conjugate palaeospreading segments for each of the four times were populated with synthetic reversal crossings via half-angle rotations of the present spreading segments around the rotation pole associated with each time. All synthetic data were spaced by 2 km.

To better simulate real data, the location of each synthetic observation was perturbed by noise drawn randomly from a Gaussian distribution centred on zero and with  $1\text{-}\sigma$  tails at  $\pm 1$  km. The synthetic magnetic reversal crossings were perturbed randomly in a direction orthogonal to their associated palaeospreading segment; fracture zone crossings were perturbed orthogonal to the local trend of the fracture zone flow line; transform fault crossings were perturbed towards or away from the best-fitting pole. The noise applied to each datum thus was a direct measure of its expected misfit. All the data were assigned uncertainties of 1 km. Consequently, a successful recovery of the four known rotations from an inversion of the noised synthetic data should have  $\hat{\kappa} = 1$ .

A simultaneous inversion of all 6600 noised synthetic data yielded a sequence of best-fitting opening poles that differ by 0.1–1.8 angular degrees from their known values and opening angles that were within 3 per cent of their known values.  $\hat{\kappa} = 0.96$  for the inversion, corresponding to an rms misfit of 1.02 km per datum. The misfits are thus only 2 per cent different than the Gaussian noise (1.0 km) that we imposed on the synthetic data. Reconstructions of the noised, synthetic data with the best-fitting rotation sequence (Fig. 6) corroborate the successful fit. Additional inversions with other realizations of the noisy synthetic data confirm that the small remaining differences between the known and estimated rotations are caused by the noise added to the synthetic data.

## 4 RESULTS

### 4.1 Reversal crossing misfits and data uncertainties

Prior to estimating best-fitting finite rotations from all the data, we subdivided the reversal crossings for all 21 reversals into three geographic subsets and separately inverted each subset to evaluate whether misfits to the reversal crossings differ significantly as a function of their location or reversal age. Fig. 7 shows the standard deviations of the misfits as a function of both reversal age and location. Misfits to the individual reversal crossings from all three geographic areas increase gradually from 1.4 km for Chron 1n to  $\approx 2$  km for Chrons 5n.1 to 6no, close to the misfits we found for both the Carlsberg Ridge (1.67 km) and Eurasia–North America Plate boundary (1.1 km) from inversions of the same reversal sequence (Merkouriev & DeMets 2006, 2008). Misfits are only slightly (5 per cent) larger for data from the more sparsely surveyed areas north of  $30^\circ\text{N}$  and south of the Kane fracture zone ( $23.5^\circ\text{N}$ ) than for the densely surveyed region between  $23.5^\circ\text{N}$  and  $30^\circ\text{N}$ .

From these results, we assign standard errors of  $\pm 1.5$  km to the densely surveyed reversal crossings from  $23.5^\circ\text{N}$  to  $30^\circ\text{N}$  for Chrons 1n to 4A and larger uncertainties of  $\pm 2.0$  km for reversals older than C4A. Uncertainties assigned to reversal crossings from  $30^\circ\text{N}$  to  $38^\circ\text{N}$  were  $\pm 1.5$  km for Chrons 1n to 2An.3,  $\pm 1.8$  km for Chrons 3n.1 to 4A and  $\pm 2.1$  km for older reversals. Reversal crossings for areas south of  $23.5^\circ\text{N}$  are  $\pm 1.5$  km,  $\pm 1.7$  km and  $\pm 2.0$  km for the same three time periods. Uncertainties were doubled for a handful of segments for which we had less confidence in our reversal correlations.

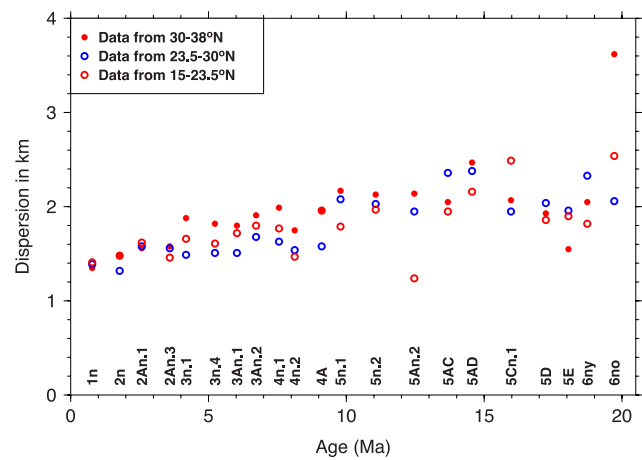


**Figure 7.** Standard deviation of the summed-squared misfits between magnetic reversal crossings and their best-fitting great circle segments as a function of reversal age and geographic location. Magnetic reversal crossings of all ages from a given geographic region are combined with fracture zone flow lines and inverted simultaneously to find the dispersion of the reversal crossings with respect to the fits of the best-fitting rotations. For reversal crossings of a given age and geographic area, the standard deviation is the square root of the summed-squared reversal crossing misfits normalized by the degrees of freedom for that rotation. The standard deviation is used to assign realistic uncertainties to the reversal crossings prior to their final inversion for the best-fitting rotation sequence.

### 4.2 Evidence and corrections for outward displacement

DeMets & Wilson (2008) previously documented evidence for 0.5–1.3 km of outward displacement along the Nubia–North America Plate boundary from  $\approx 500$  crossings of Chrons 1n to 2An.3. From our more extensive data, we re-evaluated the magnitude of outward displacement from crossings of Chrons 1n to 3n.4 (Fig. 8). We divided the reversal crossings into six geographically distinct spreading corridors (Fig. 8A). Inversions of the reversal crossings within each corridor for an assumed fixed pole gave best-fitting opening angles that we converted to total opening distances at the geographic midpoint of each spreading corridor.

Linear regressions of all six independent sequences of seafloor opening distances as a function of reversal age to estimate an opening rate and  $Y$ -intercept for each sequence gives distance–axis intercepts that range from  $-0.2$  to 1.5 km (Fig. 8B). Five of the six intercepts are greater than zero and are thus consistent with either outward displacement of the reversal boundaries or a recent spreading acceleration. In particular, regressions of the well-determined opening distances estimated from more than 2000 crossings of the well-mapped reversal sequence between  $24^\circ\text{N}$  and  $30^\circ\text{N}$  gives a narrow range of distance–axis intercepts (1.0–1.9 km) depending on which subset of reversals is used.

In order to determine whether the variation in the six distance–axis intercepts shown in Fig. 8(B) is statistically significant, we inverted all six age–distance sequences simultaneously while estimating just one, common  $Y$ -axis intercept, but six opening rates. We then compared the squared misfit for this simpler model, consisting of only seven adjustable parameters, to the summed, squared misfits for the six independent regressions described, which fit the data with a total of 12 adjustable parameters. The difference in the summed-squared misfits,  $\Delta\chi^2 = 17.4$ , fails an  $F$ -ratio test for a significant difference in fit, with only a 5 per cent probability that the latter, more complex model constitutes a significant improvement in fit relative to the fit of the model with only one  $Y$ -axis intercept.

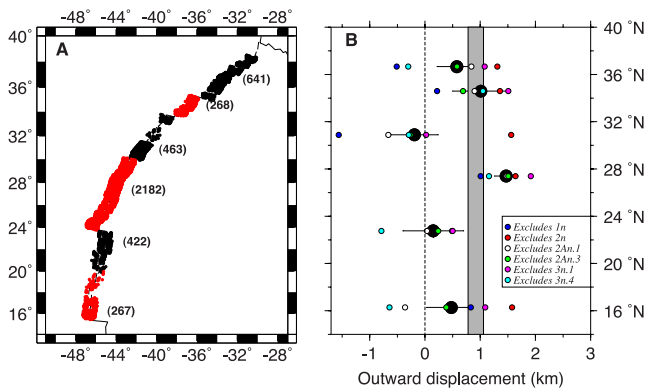


**Figure 8.** *Y*-axis intercepts (right-hand panel) from linear regressions of six opening distance time-series for Chrons 1n to 3n.4, constituting kinematic estimates of outward displacement (see text). (A) The six geographic groupings of reversal crossings used to estimate variations in outward displacement along the plate boundary. Numerals to the right of each grouping give the number of reversal crossings used to estimate the time sequence of best opening angles and best opening distances that are the basis for the analysis. (B) Black circles show the *Y*-axis intercepts determined from separate linear regressions of the six time sequences of total opening distance. Coloured circles show intercept values from regressions of the same time–distance series while excluding the opening distance for a given reversal. Excluding Chron 2n systematically increases the resulting *Y*-intercept values (red circles), whereas excluding Chron 3n.4 generally decreases the intercept values. The vertical patterned region shows the *Y*-axis intercept centred in its 1- $\sigma$  error region from a simultaneous linear regression of all six groupings. The scatter of the individual *Y*-axis intercepts about the average is not statistically significant (see text); the average value is thus used to correct for outward displacement along the entire plate boundary.

The *Y*-axis intercept from the simultaneous inversion,  $0.92 \pm 0.14$  km, thus constitutes our best estimate of outward displacement for the Nubia–North America Plate pair, although we cannot exclude the possibility that the non-zero intercept is instead evidence for a recent small acceleration in the rate of Nubia–North America seafloor spreading.

### 4.3 Best-fitting rotations, poles and lineation reconstructions

Using the procedures outlined in Section 3, we estimated two sets of finite rotations for the Nubia–North America Plate pair since 20 Ma (Tables 2 and 3). One is corrected for an assumed 1 km of outward displacement (Table 2) and accurately describes the relative motion between the two plates (i.e. their relative speed and direction of motion). The other lacks any correction for outward displacement (Table 3) and thus gives biased plate motion estimates, particularly for younger magnetic reversals. The latter rotations are useful for visual checks of the accuracy of a given reconstruction since they superimpose same-age magnetic reversals from one side of the ridge onto the other. The rotations and covariances given in both tables are determined via the bootstrapping procedure described earlier.

Except for the pole for Chron 5n.1, our new best-fitting plate motion poles are clustered within five angular degrees of  $80^\circ\text{N}$ ,  $45^\circ\text{E}$  (Fig. 9). Encouragingly, the poles for Chrons 1n, 2n and 2An.1 lie within 1.5 angular degrees of the MORVEL pole, which is derived from kinematic data that average plate motion over the same approximate interval as for the young reversals (DeMets *et al.* 2010). Opening poles for C5n.1 and C6ny estimated by Muller *et al.* (1999) from reconstructions of numerous crossings of both reversals also

lie within several angular degrees of our new estimates (Fig. 9). In a later section, we compare our new results in more detail to the predictions of the Muller *et al.*'s (1999) rotations.

The formal uncertainties in the pole locations (upper panel of Fig. 9) are similar for all 21 times, reflecting their dependence on the geometry of the reconstructed plate boundary for a given time, the number of data that define the reconstructed boundary and the data uncertainties. In contrast, the bootstrap-based rotation uncertainties (lower panel of Fig. 9) are larger, indicating that the pole locations are sensitive to the combination of segments that were selected for the data samples. Within the bootstrap uncertainties, we see no evidence for significant movement of the pole since 20 Ma.

The reconstructed magnetic reversal crossings show no first-order change in the palaeoaxial geometry relative to the present (Figs 10–12), in accord with reconstructions of Chrons 5 and 6 by Muller *et al.* (1999). Comparisons of the reconstructions for the southernmost and northernmost thirds of the plate boundary (Figs 11 and 12) to that for the central third (Fig. 10) clearly illustrates the poorer coverage for the former two relative to that for the latter, particularly for reversals older than  $\approx 10$  Ma. The more poorly constrained along-axis opening gradient for the older reversals is responsible for much of the east-to-west scatter in the estimated pole locations (Fig. 9).

Misfits of the best-fitting rotations to the individual reversal crossings obey a Gaussian distribution (Fig. 13A), are typically 2 km or less (Table 1 and Fig. 13B) and increase modestly with reversal age (Fig. 7). Over- and under-rotations of the rotated reversal crossings that define individual palaeo-axial segments relative to the stationary crossings from those segments are typically 2 km or smaller (Fig. 13C). The segment-specific systematic misfits are  $\approx 0.5$  km greater than might be expected given the dispersion of the magnetic reversal crossings, consistent with results found for the Carlsberg Ridge and Eurasia–North America Plate boundary (Merkouriev & DeMets 2006, 2008).

The stage rotations derived from the best-fitting rotations produce synthetic flow lines that closely approximate those for the three transform faults and fracture zone flow lines that were used in the inversion (Fig. 14). Weighted root-mean-square (WRMS) misfits to the transform faults are only 0.27 km (Table 1), indicating that small circles around the Chron 1n pole fit the digitized traces of the Oceanographer, Hayes and Atlantis transform faults to within 270 m at most locations. WRMS misfits to the fracture zone flow lines are only 0.37–1.46 km for the portions of the flow lines that record motion between the present and  $\approx 14$  Ma (Table 1), but increase steadily to 4.7 km thereafter. The larger WRMS misfits for portions of the flow lines that record motion before Chron 5C are almost entirely due to poor fits on both sides of the ridge to the older portions of the Atlantis fracture zone flow line (Fig. 14).

### 4.4 Validation against independent flow lines

Although we initially used the Kane fracture zone flow line as one of four flow lines that constrained our solution, doing so significantly degraded the fits to the other fracture zone flow lines and resulted in large misfits to the eastern half of the Kane fracture zone flow line. Coupled with a similarly poor fit to the azimuth of the Kane transform fault reported by DeMets *et al.* (2010), this raises concerns that deformation associated with the diffuse boundary between the North and South America plates west of the Mid-Atlantic Ridge might extend as far north as the Kane fracture zone and hence bias its direction relative to that expected for Nubia–North America motion.

**Table 2.** Nubia–North America plate motion rotations.

Chron	DOF	Lat. (°N)	Long. (°E)	$\Omega$ (degrees)	Covariances from bootstrap procedure					
					<i>a</i>	<i>b</i>	<i>c</i>	<i>d</i>	<i>e</i>	<i>f</i>
1n	971	−77.86	207.09	0.182	0.5	−0.2	−0.2	1.2	3.2	15.4
2n	964	−77.79	208.99	0.408	92.2	7.2	12.8	31.3	−3.7	22.2
2An.1	937	−78.32	211.01	0.601	41.0	−15.7	8.4	32.5	−15.6	30.2
2An.3	774	−78.74	237.97	0.782	232.0	37.0	−11.6	46.6	−17.4	29.9
3n.1	648	−78.65	224.07	0.964	372.2	127.5	−78.1	95.9	−50.0	49.3
3n.4	610	−79.29	224.81	1.176	549.8	134.6	−76.3	96.4	−46.8	44.5
3An.1	499	−79.74	227.43	1.343	364.5	−55.0	52.3	69.1	−47.9	65.0
3An.2	456	−79.85	228.27	1.504	385.2	−63.1	58.1	64.7	−34.4	72.1
4n.1	504	−80.39	225.37	1.724	554.2	46.2	−10.9	84.8	−26.4	36.7
4n.2	481	−80.48	232.45	1.858	157.0	−76.8	47.1	107.5	−60.2	76.0
4A	498	−80.93	225.32	2.172	352.5	−13.1	21.6	117.9	−67.6	77.9
5n.1	473	−79.12	259.79	2.268	880.1	136.8	−124.2	267.8	−160.4	170.2
5n.2	545	−80.97	232.83	2.664	312.9	73.5	−60.4	267.6	−175.8	171.5
5An.2	458	−80.69	238.24	3.059	111.8	−69.8	45.2	77.3	−42.0	87.1
5AC	380	−80.36	237.11	3.415	259.1	−121.0	115.9	120.1	−33.4	161.6
5AD	360	−79.86	241.65	3.716	235.5	−2.0	47.4	213.2	−21.9	105.6
5Cn.1	373	−80.14	222.31	4.210	178.8	43.3	2.1	279.0	−113.3	124.8
5D	348	−79.90	217.71	4.630	653.3	20.2	95.6	228.5	−71.3	131.1
5E	288	−79.66	215.06	4.916	262.0	111.3	−66.4	345.6	−145.6	142.3
6ny	300	−79.69	217.76	5.135	200.4	92.3	−70.7	456.7	−223.5	264.3
6no	301	−78.40	198.84	5.591	1442.7	97.3	−514.0	422.2	165.6	741.3

*Notes:* These finite rotations reconstruct movement of the Nubia Plate relative to the North America Plate and include a 1-km correction for outward displacement. The rotation angles  $\Omega$  are positive counter-clockwise (CCW). Each rotation is the mean of 2000 bootstrap solutions (see text). DOF, the degrees of freedom, equals the total number of anomaly, transform fault and fracture zone flow line crossings used to estimate the rotation for a given time reduced by the number of estimated parameters. The weighted rms misfits for these rotations are given in Table 1. The Cartesian rotation covariances are calculated in a Nubia-fixed reference frame and have units of  $10^{-10}$  radians<sup>2</sup>. Covariances are determined from the bootstrapping procedure described in the text. Elements *a*, *d* and *f* are the variances of the (0°N, 0°E), (0°N, 90°E) and 90°N components of the rotation. The covariance matrices are reconstructed as follows:

$$\begin{pmatrix} a & b & c \\ b & d & e \\ c & e & f \end{pmatrix}.$$

We therefore opted to exclude the Kane transform fault from our inversion for Nubia–North America rotations and instead use its flow line to evaluate the latitudinal extent of deformation between the North and South America plates. As is described later, we find little evidence that deformation extends as far north as the Kane fracture zone.

Fig. 15 shows flow lines that are predicted for the Kane and Fifteen-Twenty fracture zones on the Nubia and North America plates from the same stage rotations that are used to construct the flow lines for the Atlantis, Hayes and Oceanographer fracture zones. West of the Mid-Atlantic ridge, the flow line predicted for the Kane fracture zone lies entirely within the well-defined fracture zone valley. East of the ridge, the predicted flow line is located  $\approx 5$  km south of the valley within  $\approx 100$  km of the ridge-transform intersection (Fig. 15), but is otherwise located within the valley. Diffuse deformation between the North and South America plates cannot be the cause of the  $\approx 5$ -km systematic misfit east of the ridge since any such deformation would instead occur west of the ridge. The misfit might instead be evidence for slow northward propagation of the spreading segment that terminates the eastern end of the Kane transform fault.

The flow line predicted for the Fifteen-Twenty fracture zone west of the ridge also lies entirely within the fracture zone valley, as does most of the predicted flow line east of the ridge (lower panel of Fig. 15). The good fit, particularly west of the ridge, is unexpected

given evidence that at least some deformation between the North and South America plates occurs north of the Fifteen-Twenty fracture zone (Roest & Collette 1986). Our results suggest that diffuse deformation between North and South America does not extend as far north as the Kane fracture zone, and may indicate that the N–S component of deformation (i.e. the component orthogonal to the fracture zones) between the two plates is a few kilometres or less even as far south as the Fifteen-Twenty fracture zone.

#### 4.5 Plate motion synthesis

Fig. 16 summarizes seafloor spreading rates and directions since 20 Ma at the midpoint of the plate boundary, where the plate motion is best determined due to the numerous, easily interpreted magnetic reversal crossings (Fig. 3). Since 6 Ma, interval rates have averaged  $22 \pm 0.5$  mm yr<sup>−1</sup> (Fig. 16A) and are consistent with steady seafloor accretion within their estimated uncertainties. Four of the post-6 Ma interval rates that are determined from completely independent sets of magnetic reversal crossings (i.e. C1n to the present; C2n to the present; C3n.1 to C2An.1; C3n.4 to C2An.3) agree with each other within 1 mm yr<sup>−1</sup>, offering strong evidence for the accuracy and precision of our newly estimated finite rotations for these times.

Prior to  $\approx 8$  Ma, the interval spreading rates averaged  $29 \pm 2$  mm yr<sup>−1</sup>, roughly 30 per cent faster than the present rate.

**Table 3.** Nubia–North America reconstruction rotations.

Chron	Lat. (°N)	Long. (°E)	$\Omega$ (degrees)	$a$	Covariances from single inversion					
					$b$	$c$	$d$	$e$	$f$	
1n	-77.91	208.30	0.187	16.8	-13.7	13.9	12.0	-11.8	12.0	
2n	-77.95	218.14	0.410	69.1	-59.7	46.5	52.7	-39.9	34.0	
2An.1	-78.35	212.72	0.609	70.2	-58.8	47.2	50.7	-39.7	34.8	
2An.3	-78.46	241.70	0.786	97.7	-81.9	68.6	70.2	-57.6	51.9	
3n.1	-78.93	226.90	0.972	147.6	-126.4	99.5	110.8	-85.4	72.1	
3n.4	-79.23	229.57	1.177	179.4	-152.7	119.8	131.9	-101.9	85.9	
3An.1	-79.77	228.34	1.352	234.7	-196.0	150.3	167.7	-127.0	104.2	
3An.2	-79.77	229.69	1.512	280.5	-239.6	184.4	208.7	-158.2	129.0	
4n.1	-80.29	225.79	1.729	254.6	-212.3	165.1	180.7	-138.8	115.2	
4n.2	-80.50	235.16	1.859	316.8	-268.6	205.2	233.1	-176.2	141.7	
4A	-80.85	226.04	2.180	331.8	-289.8	227.1	256.3	-197.8	167.1	
5n.1	-79.19	259.32	2.283	453.2	-395.3	309.4	348.5	-270.1	224.7	
5n.2	-81.03	232.17	2.678	265.4	-232.4	184.6	206.9	-161.4	139.1	
5An.2	-80.64	239.13	3.066	312.7	-277.9	223.5	249.8	-196.3	173.7	
5AC	-80.28	238.67	3.420	361.4	-324.2	259.7	295.0	-229.3	202.7	
5AD	-79.78	242.76	3.717	471.4	-425.2	336.5	387.9	-299.2	258.3	
5Cn.1	-80.22	223.71	4.215	443.2	-392.3	312.1	352.5	-274.3	237.4	
5D	-79.96	219.99	4.622	418.8	-378.8	281.8	349.3	-252.4	207.5	
5E	-79.73	216.86	4.913	533.7	-488.1	362.7	455.7	-329.7	265.9	
6ny	-79.74	219.21	5.137	491.4	-438.2	337.4	399.0	-300.1	253.1	
6no	-78.52	200.06	5.592	1395.0	-1251.0	1092.7	1138.4	-972.7	885.6	

Notes: These finite rotations reconstruct reversals on the Nubia Plate onto their counterparts on the North America Plate and do not include any corrections for outward displacement. The rotation angles  $\Omega$  are positive CCW. Rotations and their covariances are determined from a single inversion of all the data. Table 2 specifies the degrees of freedom per rotation. Cartesian rotation covariances are calculated in a Nubia-fixed reference frame and have units of  $10^{-10}$  radians<sup>2</sup>. See Table 2 caption for further information.

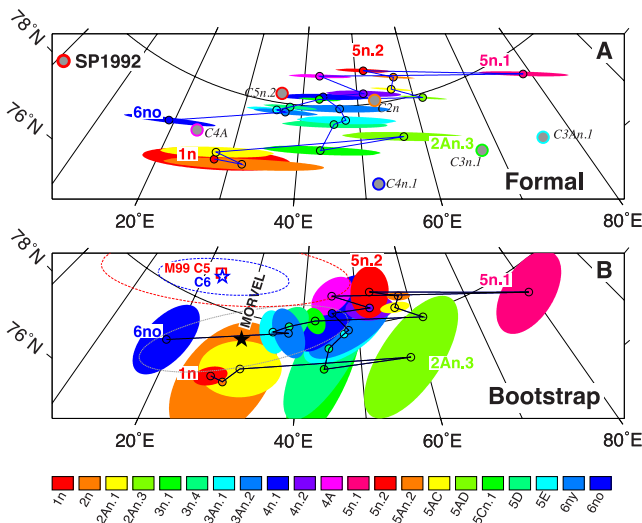


**Figure 9.** Nubia–North America plate motion poles and their 2-D 95 per cent confidence regions for Chrons 1n to 6no (Table 2). (A) Formal confidence limits from single data inversion and covariances determined from the geometry of the palaeoplate boundary and number of data. Confidence limits do not account for correlations between the finite rotations introduced by the fracture zone flow line data. Grey-shaded circles are from table 1 of Sloan & Patriat (1992) and are labelled by the reversal they reconstruct. (B) Pole locations and confidence limits from bootstrapping procedure described in the text. Star shows the 3-Myr-average MORVEL Nubia–North America pole and its 95 per cent confidence ellipse (grey line), Square and star labelled ‘M99 C5’ and ‘C6’ show locations of Muller *et al.* (1999) opening poles for Chrons 5n.1 and 6ny and their 2-D 95 per cent confidence regions.

By implication, a significant slowdown in the spreading rate occurred after 8 Ma and before 5 Ma. Below, we test rigorously for the timing and duration of this spreading slowdown. For times before 9 Ma, the interval rates are scattered 3–4 mm yr<sup>-1</sup> about the average rate, presumably due to the sparser shipboard coverage of the older magnetic anomalies and possible errors in our reversal correlations for some spreading segments. Later, we employ Monte Carlo sampling to test whether the larger scatter for the older reversals is attributable to these factors.

The smoothly changing plate slip directions since 20 Ma (Fig. 16B) are an outcome of our flow-line inversion procedure, which encourages best-fitting finite rotation sequences that satisfy flow-line continuity. From 19 to 8 Ma, the estimated slip direction rotated slowly anticlockwise by  $\approx 7$  degrees. Since  $\approx 7$  Ma, the slip direction has rotated slowly clockwise to the direction dictated by the present-day transform faults. Encouragingly, Sloan & Patriat (1992) also describe evidence for a change in direction at 7 Ma based on their analysis of dense data from the SARA survey region (28–29°N).

4.5.1 Comparison to MORVEL and GPS estimates of present Nubia–North America motion

The 3 Myr average opening rate estimated from the MORVEL Nubia–North America angular velocity is  $22.9 \pm 0.3$  mm yr<sup>-1</sup> (Fig. 16A), only 3 per cent faster than indicated by our analysis. The plate slip direction estimated with MORVEL differs by only 1° from the post-5 Ma interval slip directions predicted by our plate motion rotations (Fig. 16B). The good agreement between the MORVEL and our new estimates is encouraging, but not unexpected given that they are derived from many of the same data.

A simultaneous inversion of the 1343 Nubia and North America Plate GPS site velocities gives an angular velocity of 83.9°N,

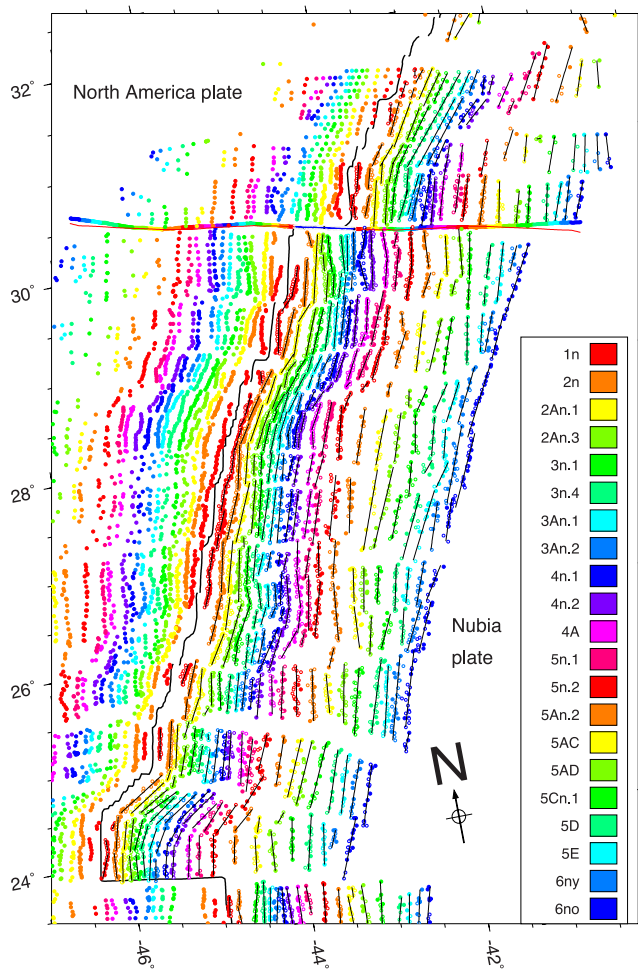


**Figure 10.** Best-fitting Nubia–North America reconstructions, 24–32°N. Filled circles show reversal crossings at their original locations from Fig. 3. Open circles show North America Plate magnetic reversal crossings reconstructed to their positions on the Nubia Plate by the best-fitting rotations in Table 2. Bold line shows axis of the Mid-Atlantic Ridge. Thin black lines show best-fitting great circle segments for the stationary and rotated reversal crossings that define each reconstructed spreading segment. Projection is oblique Mercator around a pole at 80°N, 40°E, near the centre of the best-fitting Nubia–North America poles.

23.8°E and 0.228°/Myr for the instantaneous motion of the Nubia Plate relative to North America. This angular velocity predicts that the Nubia–North America seafloor spreading rate at the boundary midpoint has been  $22.1 \pm 0.2 \text{ mm yr}^{-1}$  for the past decade, remarkably similar to our independently estimated long-term rate of  $22.2 \pm 0.5 \text{ mm yr}^{-1}$  (Fig. 16A). Extrapolating the GPS-based estimate to the past 0.781 Myr (Chron 1n), the GPS angular velocity predicts that 15.0 km of new seafloor has been created at the northern end of the plate boundary and 18.9 km at the southern end. At the same respective locations, the Chron 1n rotation (Table 2) predicts total seafloor accretion of 14.7 and 19.0 km since 0.781 Ma. The 100- to 300-m differences in the Chron 1n and GPS-extrapolated opening distances are smaller than the  $1\text{-}\sigma$  uncertainty of  $\pm 500 \text{ m}$  that we estimate for the 1-km correction we make for outward displacement (Fig. 8). Consequently, decreasing the correction we make for outward displacement by  $\approx 200 \text{ m}$  would reduce the difference between the GPS and Chron 1n estimates to negligible values.

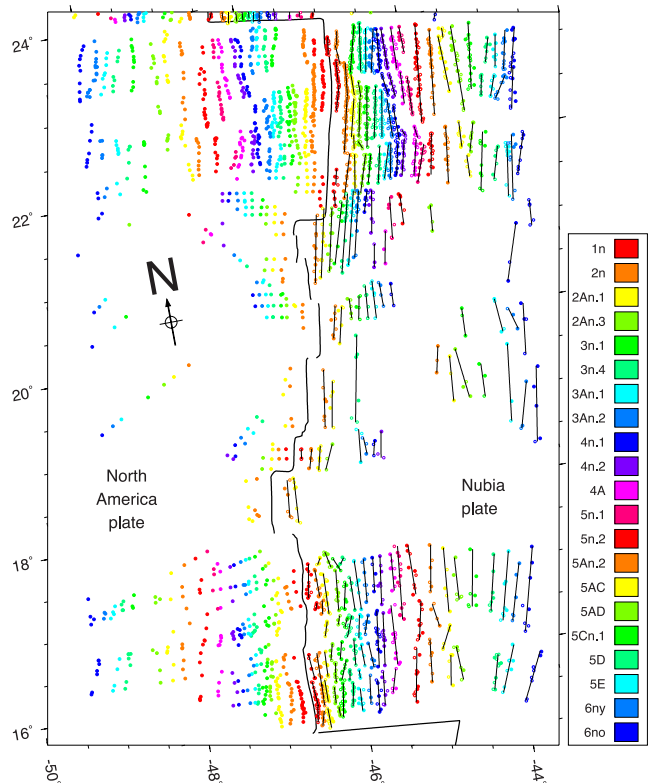


**Figure 11.** Best-fitting Nubia–North America reconstructions, 15–24°N. Filled circles show reversal crossings at their original locations from Fig. 3. Open circles show North America Plate magnetic reversal crossings reconstructed to their positions on the Nubia Plate by the best-fitting rotations in Table 2. Bold line shows axis of the Mid-Atlantic Ridge. Thin black lines show best-fitting great circle segments for the stationary and rotated reversal crossings that define each reconstructed spreading segment. Projection is oblique Mercator around a pole at 80°N, 40°E, near the centre of the best-fitting Nubia–North America poles.

Although the GPS and Chron 1n rotations predict similar seafloor spreading rates, the GPS-derived pole is 6.0 angular degrees north of the poles for Chron 1n and the other young reversals, well outside their confidence regions (Fig. 9). The GPS pole predicts present-day plate slip directions that are 6–7° anticlockwise of the well-mapped traces of the Oceanographer, Atlantis and Hayes transform faults and of the directions predicted by the Chron 1n and MORVEL Nubia–North America poles (Fig. 16B).

Given the poor fit of our GPS pole to the Nubia–North America directions, we explored whether previously published GPS estimates of the Nubia–North America angular velocity reduce the misfit to acceptable levels. None do. In order of publication, the Nubia–North America angular velocities from Sella *et al.* (2002), Altamimi *et al.* (2007), Kogan & Steblov (2008) and Argus *et al.* (2010) are located 15.1°, 7.1°, 11.4° and 8.7° from our Chron 1n pole, all farther away than our newly estimated pole. All predict present-day slip directions that are 4–7° anticlockwise of the well-mapped plate boundary transform faults, larger than the  $\pm 1.1^\circ$  to  $1.3^\circ$  uncertainties estimated for the transform fault azimuths (DeMets *et al.* 2010). None of the GPS estimates, including our own, correctly predicts the transform fault trends even though the GPS estimates use three different realizations of ITRF, different corrections for systematic biases in the geodetic site velocities and different sets of GPS site velocities.

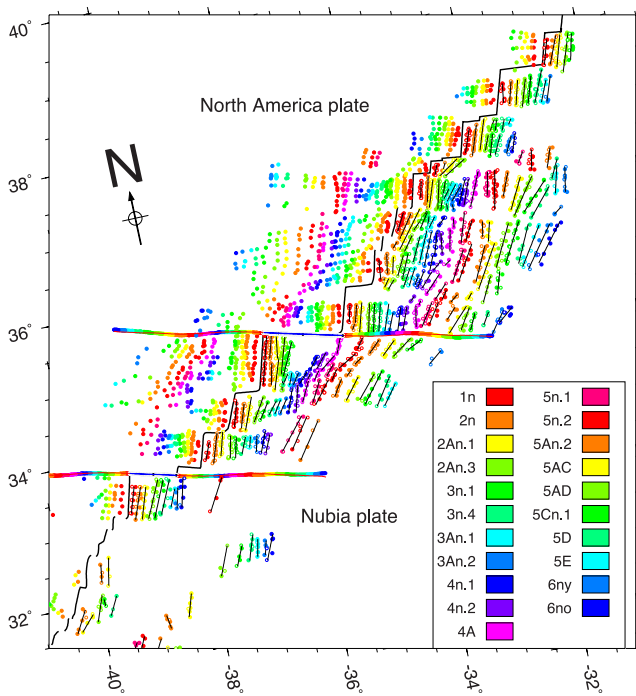


**Figure 12.** Best-fitting Nubia–North America reconstructions, 32–38°N. Filled circles show reversal crossings at their original locations from Fig. 3. Open circles show North America Plate magnetic reversal crossings reconstructed to their positions on the Nubia Plate by the best-fitting rotations in Table 2. Bold line shows axis of the Mid-Atlantic Ridge. Thin black lines show best-fitting great circle segments for the stationary and rotated reversal crossings that define each reconstructed spreading segment. Projection is oblique Mercator around a pole at 80°N, 40°E, near the centre of the best-fitting Nubia–North America poles.

Our new and previously estimated Nubia–North America GPS angular velocities predict that Nubia–North America motion has rotated 4–7° anticlockwise since 0.78 Ma or possibly over the past few Myr. If this were true, the change in direction would have placed the left-slipping, eastward-stepping Oceanographer, Atlantis and Hayes transform faults under oblique transpression and the right-slipping, westward-stepping Kane transform fault under oblique extension. However, none of these transform faults have developed structures such as intratransform pull-apart basins or high median ridges that typically form along transform faults with obliquely divergent or obliquely convergent slip. If the change in the slip direction were recent enough, such structures may not have formed yet. Alternatively, the absence of these structures suggests that the GPS estimates are in error.

The GPS site velocities from the North America and Nubia plates are too numerous and too well determined (Figs 4 and 5) for random errors to be responsible for the misfit in direction. Systematic errors must thus be invoked. For example, glacial isostatic rebound may bias a subset of our North America GPS site velocities (Calais *et al.* 2006; Sella *et al.* 2007), most likely in the northern United States, where the effect is the largest. We tested this hypothesis by inverting Nubia and North America Plate velocities after excluding the velocities of 534 North America Plate sites in the northernmost US states. The modified Nubia–North America angular velocity lies 0.7 angular degrees closer to the pole for Chron 1n and predicts slip directions that are 0.7° closer to the observed transform fault trends than for the angular velocity determined from the larger

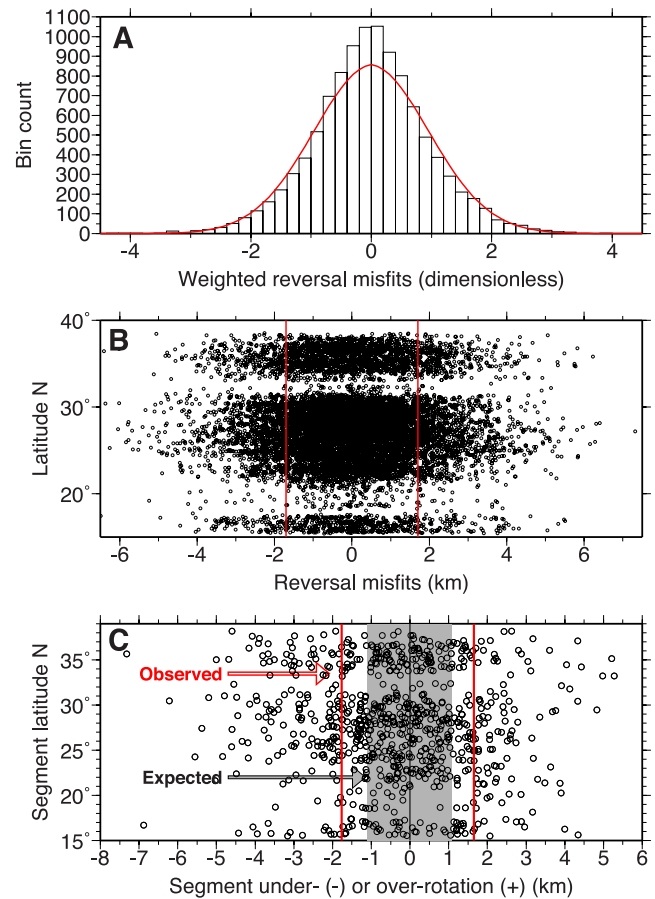


**Figure 13.** Data misfits. (A) Histogram of misfits for 10 769 reconstructed Nubia–North America reversal crossings for Chrons 1–6no normalized by their estimated uncertainties. Red curve shows the distribution of weighted residuals expected for an equivalent number of degrees of freedom (10 769 minus 1674, the number of fitting parameters) assuming the data have normally distributed errors and the uncertainties are estimated correctly. (B) Residual distances from (A) versus plate boundary latitude. Red lines encompass 68.3 per cent of the residuals adjusted by the number of estimated parameters and thus approximate the dispersion of the reversal crossings relative to their best-fitting great circle segments. (C) Over- and under-rotations of the 816 rotated reversal segments with respect to their fixed-side segment counterparts for Chrons 1–6no. The dispersion (red lines) for the observed segment misfits exceeds the misfits expected for reversal crossings affected solely by random errors (shaded area), indicating that the reversal locations are influenced by systematic errors from a variety of possible sources such as reversal misidentifications and segment-to-segment variation in the magnitude of outward displacement.

number of data. Although this does not resolve the full difference between the geological and geodetic plate motion estimates, it suggests that glacial isostatic rebound is at least partly responsible for the difference between the two.

Slow deformation within the southwestern United States might also bias our North America Plate angular velocity. Similarly, slow deformation of the Nubia Plate near its wide boundaries with the Eurasia and Somalia plates might bias our estimate of the Nubia Plate angular velocity. Finally, uncertainties in the translational motion of the Earth’s centre as realized in ITRF may bias all the GPS site velocities and plate angular velocity estimates, as documented by Argus (2007). Further work on all the above-mentioned is clearly warranted, but exceeds the scope of this study.

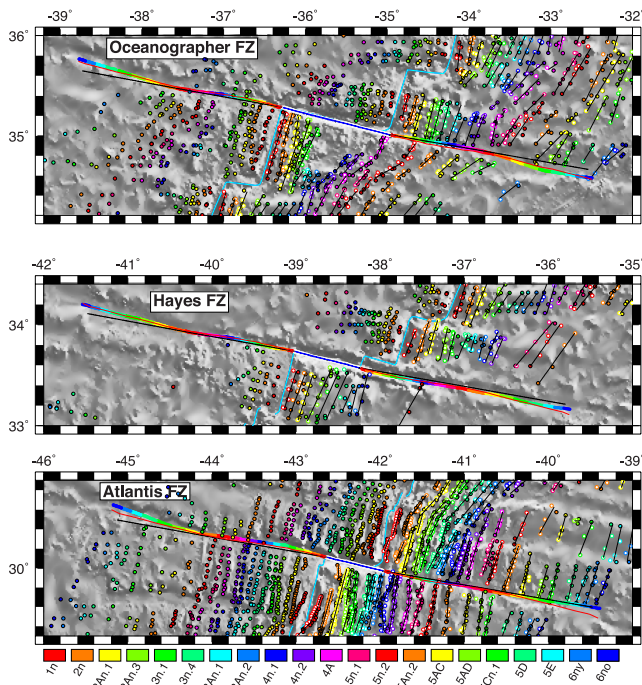


**Figure 14.** Reconstructed best-fitting flow lines (red lines), transform faults (blue lines) and nearby reversal crossings for each of the three fracture zones used to estimate the best-fitting Nubia–North America rotations (Table 2). Black lines are flow lines determined from the Muller *et al.* (1999) rotations for Chrons 5n.1 and 6ny. Black circles show transform fault crossings digitized from multibeam surveys of the three transform faults. Fracture zone flow line crossings (variously coloured circles) are digitized from GeoMapApp multibeam bathymetry and gravity-based seafloor topography. Colour coding of each flow line crossing indicates the particular finite rotation that the datum constrained within the inversion. Magnetic reversal crossings indicated with filled symbols are at their original location, whereas those shown with open symbols are rotated onto the Nubia Plate using the best-fitting finite rotations.

## 4.6 Timing and suddenness of change in spreading rate

### 4.6.1 Synthetic spreading history example

We next use the stage spreading rates to find best estimates for the timing and duration of the spreading slowdown illustrated in Fig. 16(A). The interval rates estimated at the geographic centre of the plate boundary are well suited for this test because they are well constrained by the densely surveyed, precisely dated magnetic reversal sequence from 24°N to 30°N (Fig. 3). As part of our analysis, we also use Monte Carlo simulations of the interval spreading history to evaluate whether the scatter in the observed interval rates is consistent with the known uncertainties in the reconstructed opening distances and the small but non-zero uncertainties in the astronomically tuned reversal ages.

Before working with the observed stage spreading rates, we first evaluated what information can be recovered from synthetic stage spreading rates based on a hypothetical spreading history in which steady seafloor spreading at a rate of 29 mm yr<sup>-1</sup> from 20 to 7 Ma decreases suddenly at 7 Ma to 22 mm yr<sup>-1</sup> and remains unchanged to the present (shown by the red line in Fig. 17). Based on this spreading history, we created a sequence of synthetic seafloor opening distances for all 21 reversals given in Table 1 and from them determined interval spreading rates (red circles in Fig. 17) for the same time intervals as for our observed interval rates (Fig. 16A).

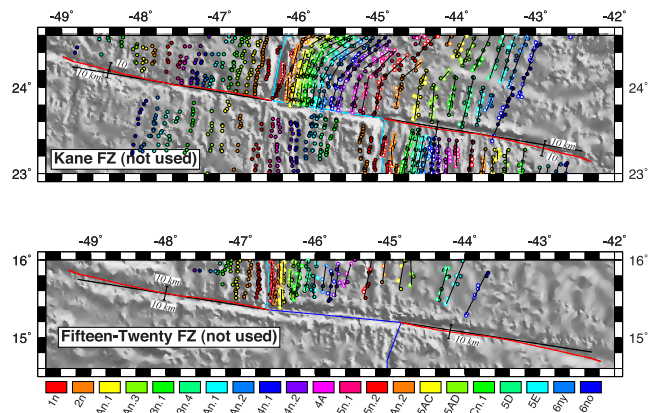


**Figure 15.** Predicted flow lines (red and black lines) for the Kane and Fifteen-Twenty fracture zones overlaid on bathymetry from GeoMapApp (Carbotte *et al.* 2004). Red lines show flow lines predicted by stage rotations determined from best-fitting Nubia–North America rotations (Table 2). Black lines are flow lines predicted from the Muller *et al.* (1999) rotations for Chrons 5n.1 and 6ny. Magnetic reversal crossings shown by filled symbols are in place, whereas those shown with open symbols have been rotated onto the Nubia Plate by the best-fitting finite rotations. 10-km distance markers perpendicular to each flow line are shown for scale east and west of the ridge.

Contrary to the sudden decrease in spreading rates that is imposed in our spreading-rate model, the synthetic interval rates decrease gradually between  $\approx 8$  and 5.5 Ma (Fig. 17). As expected, discrete sampling of the continuous seafloor spreading history at intervals spaced every 1–2 Myr yields a smoothed spreading history that masks sudden changes in motion. Although sampling the seafloor distances more frequently would give interval spreading rates that better approximate the timing and duration of the change in spreading rate at 7 Ma, it would also increase the noise in the estimated stage rates via the well-known trade-off between resolution and noise. Given our original objective of determining palaeospreading rates to the nearest mm yr<sup>-1</sup>, the uncertainties in our estimated finite rotations impose a practical lower limit of  $\approx 1$  Myr for the duration of the time intervals we use to estimate stage opening rates.

Using the same synthetic seafloor opening distances, we also explored how noise influences our ability to extract information about the spreading slowdown. We added random noise to both the synthetic opening distances and the magnetic reversal ages via Monte Carlo sampling of Gaussian probability distributions with assumed 1- $\sigma$  widths of  $\pm 2$  km for the opening distances and  $\pm 20\,000$  yr for the reversal ages. These 1- $\sigma$  widths are 1.5–2 times larger than the noise we estimate for our reconstructed opening distances and the astronomically tuned reversal ages and thus constitute a worst-case analysis of the scatter in the recovered interval-rate histories.

Via repeated sampling of the Gaussian noise, we constructed 50 sequences of 21 noisy opening distances and their corresponding, noisy reversal ages. For each sequence, we then determined interval spreading rates using the same time intervals as for our real stage spreading rates. The resulting synthetic stage spreading histories (grey lines in Fig. 17) illustrate the expected scatter in the estimated interval rates given the assumed noise in the opening distances and reversal ages. The ensemble of noisy spreading histories recover the spreading deceleration despite the conservative assumptions we made about the underlying noise. By implication, our Nubia–North America finite rotations should be determined well enough to recover any change in motion with high confidence.

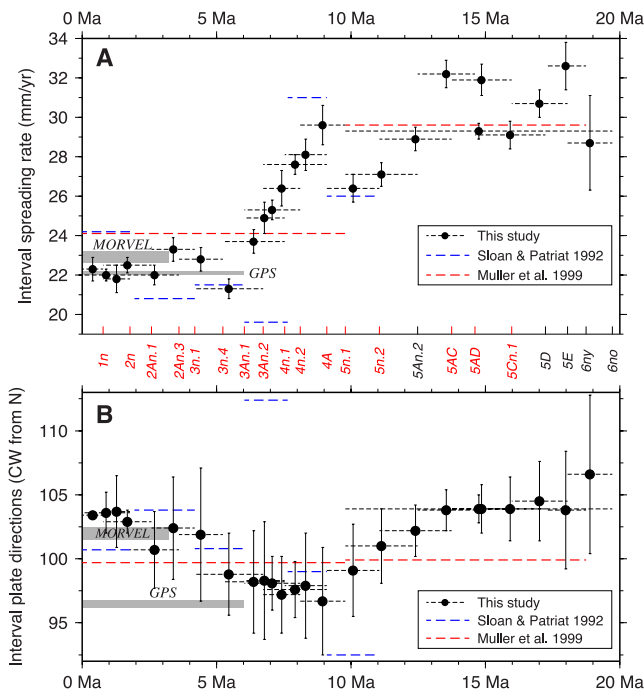


**Figure 16.** Nubia–North America seafloor spreading rates (A) and plate slip directions (B) for time intervals shown by horizontal dashed lines. Stage rotations derived from the plate motion rotations (Table 2) are used to predict motion at  $27.4^{\circ}\text{N}$ ,  $44.4^{\circ}\text{W}$ , near the geographic midpoint of the plate boundary.  $1\text{-}\sigma$  uncertainties are propagated from the rotation covariances. Grey bars show opening rates and directions predicted by the MORVEL Nubia–North America 3.2-Myr-average angular velocity (DeMets *et al.* 2010) and a new GPS-based angular velocity (this study). Coloured lines show predictions of stage rotations from Sloan & Patriat (1992) and Muller *et al.* (1999) at the same location after correcting for outward displacement and applying reversal ages from Hilgen *et al.* (2012). Reversal identifiers between the panels are lettered in red for reversals whose age estimates are astronomically tuned and in black for reversals whose ages are estimated via minimization of Pacific Basin seafloor spreading rate changes in the mid-Miocene (Hilgen *et al.* 2012).

#### 4.6.2 Nubia–North America spreading history

We next evaluate the Nubia–North America spreading rate history (Fig. 16A) using the above-mentioned procedures, with an objective of finding best estimates for the timing of the spreading slowdown and its duration. The plate motion rotations and bootstrap covariances given in Table 2 are used to find the opening distance and realistic uncertainty for each reversal for a point at  $27.4^{\circ}\text{N}$ ,  $44.4^{\circ}\text{W}$ . Uncertainties of  $\pm 5\,000$  yr were assigned to the uninterrupted astronomically tuned reversal sequence from Chrons 1n through 5An.2. Reversal age uncertainties were increased to  $\pm 10\,000$  yr to  $\pm 50\,000$  yr for the partially tuned age estimates for Chrons 5AC to 6no.

To identify a best-fitting interval spreading history, we constructed a series of alternative spreading histories in which spreading rates changed as early as 8 Ma or as recently as 6.5 Ma (see inset to Fig. 18) and in which the duration of the slowdown ranged from instantaneous (0.0 Myr curve in the inset to Fig. 18) to 1.5 Myr. The stage spreading rates determined for each of the alternative spreading histories were compared to the observed stage rates (shown by the black circles in Fig. 18) to identify the spreading history that minimizes the weighted least-squares difference between the two.

The spreading history that minimizes the misfit consists of a spreading rate slowdown that started at 8.2 Ma and ended at 6.2 Ma

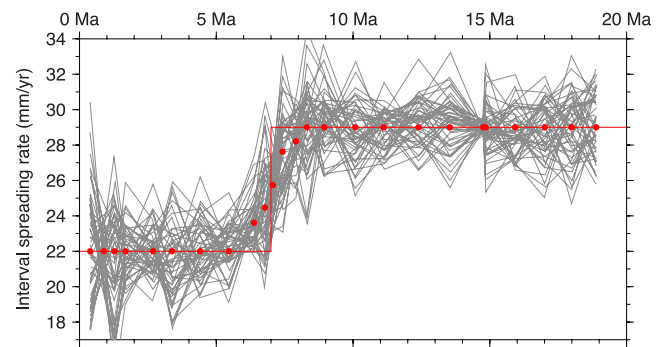


**Figure 17.** Demonstration of expected interval spreading rates and interval rate scatter for a known interval rate model (red line) in which steady-state seafloor spreading before 7 Ma decelerates abruptly at 7 Ma and remains the same to the present (see text). Red circles show interval rates determined from the synthetic opening distance time-series for this spreading-rate model using the same age intervals as are used to determine the observed interval rates shown in Fig. 16. The instantaneous rate change is manifested as a gradual change over 2 Myr, reflecting the discrete sampling. Grey lines show 50 realizations of the interval-rate history from Monte Carlo sampling of Gaussian probability error distributions for the reversal ages and reconstructed opening distances assuming uniform 20 000-yr standard errors for the former and 2-km standard errors for the latter observations (see text). The grey lines indicate the expected level of scatter in the estimated interval rates given the noise assumed for the observations.

(red line in Fig. 18). The stage rates predicted by this model (red circles in Fig. 18) correctly reproduce the pattern of observed rates from 9 to 6 Ma, when rates were changing. For comparison, a hypothetical spreading history that imposes an instantaneous spreading slowdown at 7.0 Ma (open blue circles in the same figure) produces stage spreading rates that clearly misfit the observed rates from 9 to 6 Ma. Relative to the best model, spreading histories that assume decelerations before 7.5 Ma or after 7.0 Ma are rejected at the 95 per cent confidence level, as are histories with instantaneous decelerations that begin before 7.3 Ma.

Monte Carlo sampling of the noise in the data and magnetic reversal ages, as described in Section 4.6.1, yields a suite of interval rates (grey lines in Fig. 18) that encompass all of the observed interval rates. In particular, all the interval rates for times since 10 Ma lie well within the extrema of the Monte Carlo realizations, indicating that the bootstrap rotation covariances adequately capture the uncertainty in the opening distances. In contrast, half of the interval rates for times before 10 Ma lie near the extrema of the Monte Carlo realizations, suggesting that either the bootstrap covariances understate the true opening distance uncertainties, the reversal age uncertainty estimates are too small, or some combination thereof. The three most likely causes for the underestimated uncertainties in the older rotations are misidentifications of Chrons 5AC and 5D within the sequence of short reversals that comprise Chrons 5AA to 5B (Fig. 2), misidentifications of Chron 5C, which is often poorly expressed in our study area, and incorrect identifications of some older magnetic reversals in the more sparsely surveyed areas at the north and south ends of the plate boundary.

## 5 DISCUSSION AND CONCLUSIONS

### 5.1 Comparison to Sloan & Patriat (1992) results

We compared the motions predicted by our newly estimated rotations to those predicted by two previous studies, one based

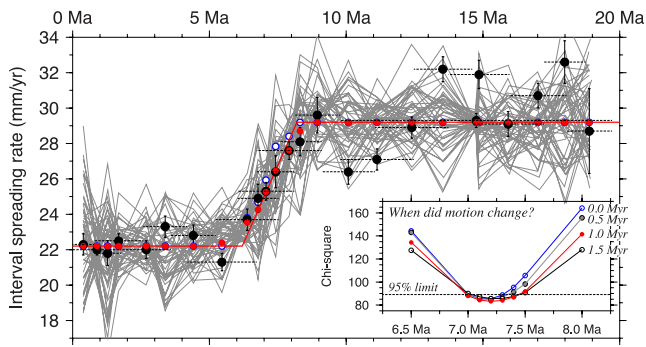


**Figure 18.** Best estimates of timing and duration of change in Nubia–North America interval rates. Inset panel shows least-squares misfits of alternative models for the interval spreading-rate history to the observed interval spreading rates from Fig. 16. Two parameters are varied per model—the midpoint age of the time interval during which the spreading rate changed and the duration of the interval during which the spreading rates decelerated. Circles indicate the midpoint ages that were tested and coloured curves and circles show the influence of the interval duration on the fit (ranging from instantaneous—0.0 Myr—to gradual—1.5 Myr). Dashed line indicates 95 per cent confidence limit relative to best-fitting model as determined from a chi-square test for two adjustable parameters. In the main panel, the red line shows the best-fitting model, in which steady-state seafloor spreading before 7.7 Ma decelerates gradually until 6.7 Ma, after which spreading rates remain the same to the present. Red symbols show interval rates determined from the best-fitting model for the same time intervals (black dashed lines) as for the observed interval rates (black circles). Open blue circles show stage rates for a worse-fitting model in which the rate slowdown is forced to occur instantaneously at 7.0 Ma. Grey lines show 50 Monte Carlo realizations of the best-fitting interval rate model determined by Monte Carlo sampling of realistic Gaussian probability error distributions for the reversal ages and reconstructed opening distances (see text). The observed interval rates fall within the envelope of the Monte Carlo realizations, suggesting that the variations in the observed rates are consequences of errors in the estimated reversal ages and opening distances.

principally on a detailed analysis of dense magnetic data from young seafloor between 28°N and 29°N (Sloan & Patriat 1992) and the other based on reconstructions of Chrons 5n.1 and 6ny along the whole plate boundary (Muller *et al.* 1999). Although McQuarrie *et al.* (2003) also estimate Nubia–North America Plate rotations, we opted not to compare our results to their analysis because their reconstructions are based on earlier magnetic reversal correlations of Klitgord & Schouten (1986), which we consider to be superseded by those of Muller *et al.* (1999).

Sloan & Patriat (1992) estimate finite rotations for magnetic reversals 2ny, 3n.1, 3An.1, 4n.1, 4A and 5n.2 from dense magnetic data from 28°N to 29°N. Surprisingly, all of their rotation poles are located within several angular degrees of our own poles (upper panel of Fig. 9), even though Sloan and Patriat used data from only an ≈100-km-long segment of the plate boundary. Fig. 16(A) compares stage rates determined from our best-fitting rotations (Table 2) to stage rates that we determined from the Sloan & Patriat stage rotations. For consistency, we used reversal ages from Hilgen *et al.* (2012) to determine their interval spreading rates and corrected their interval rates for 1 km of outward displacement. The resulting sequence of stage spreading rates clearly shows an ≈25 per cent spreading slowdown at 7 Ma, as reported in their study.

The stage slip directions predicted from Sloan and Patriat's stage rotations agree within 2–3° of our own for times since 6 Ma (Fig. 16B) and crudely confirm the ≈5° clockwise change in slip di-

rection defined by our slip directions between 7 Ma and the present. We suspect that the ≈15° difference between our estimated slip directions from 7.5 to 6 Ma is a consequence of the restricted area from which their data are taken and the different method they use to estimate finite rotations.

That our rotation poles are more tightly clustered than those of Sloan and Patriat (Fig. 9) and our interval spreading rates and directions define simpler, more consistent patterns (Fig. 16) suggests that our new rotations improve on those estimated by Sloan and Patriat. This is expected given that our data span the length of the entire plate boundary and outnumber the data they used by an order of magnitude or more (Table 1 and Figs 10–12).

## 5.2 Comparison to Muller *et al.* (1999) results

Muller *et al.*'s (1999) reconstructions of magnetic reversals 5n.1 and 6no are based on their correlations of these reversals along the entire plate boundary. At 27.4°N, where the rotations for Chrons 5n.1 and 6ny for both studies are strongly constrained by dense magnetic coverage, the total opening predicted by Muller *et al.*'s rotations differs by only 0.4 and 1.8 km from that predicted by our rotations. Differences in total opening predicted by the two studies at the northern and southern ends of the plate boundary are as large as 10.3 km, reflecting the sparser magnetic survey coverage and greater difficulty in identifying the older magnetic anomalies in these areas (see in particular Fig. 11).

The Muller *et al.* rotations predict that opening rates since Chron 5n.1 (9.786 Ma) have averaged 24 mm yr<sup>-1</sup>, 10 per cent faster than our own estimate of the opening rate that has prevailed since ≈5 Ma (Fig. 16A). However, the Muller *et al.*'s estimate encompasses the periods of faster spreading before ≈8 Ma and slower spreading since 6 Ma and thus fails to predict the spreading rate for either period. Encouragingly, our two studies predict remarkably similar spreading rates from 19 to 9 Ma (Fig. 16A), 29.3 ± 0.2 mm yr<sup>-1</sup> for our study versus 29.6 mm yr<sup>-1</sup> for that of Muller *et al.*

The principal difference between our and Muller *et al.*'s (1999) estimates of the C5n.1 and C6ny rotations are revealed by the different synthetic flow lines that the two predict. West of the Mid-Atlantic ridge, the flow lines predicted by the Muller *et al.* (1999) rotations are located systematically south of the well-defined fracture zone valleys for seafloor ages older than Chron 5n.1 (Figs 14 and 15). The difference in the observed and predicted flow line locations increases from negligible values (under 1 km) for Chron 5n.1 to as much as 20 km for the oldest (western) ends of the flow lines. These differences are caused partly by the different fracture zones that are used to constrain the two sets of rotations. Muller *et al.* (1999) reconstruct the Kane and Atlantis fracture zones, as interpreted from satellite-derived gravity data available in 1999. We use the Oceanographer, Atlantis and Hayes fracture zones, as digitized from a combination of multi- and single-beam bathymetry complemented by bathymetry derived from satellite gravity data.

Not surprisingly, the stage directions predicted from the Muller *et al.*'s stage rotations (red dashed lines in Fig. 16B) describe a slip history different than derived herein. The simpler slip history implied by the Muller *et al.*'s study misses the change in direction at 7–8 Ma that is indicated by our stage rotations and those of Sloan & Patriat (1992), and more poorly fits the small circle traces of the plate boundary transform faults than our own rotations.

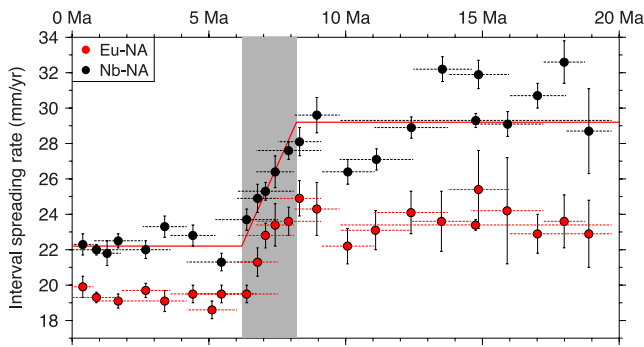


**Figure 19.** Nubia–North America interval rates from this study (black circles) and Eurasia–North America interval rates from Merkouriev & DeMets (2008; red circles) for the same stage intervals. Shaded bar delineates decelerating Nubia–North America spreading rates from 8.2 to 6.2 Ma, as determined from an analysis of the stage spreading history described in the text. Red line indicates the best three-stage spreading history from the same analysis. Nubia–North America stage rates are determined near the boundary midpoint (27.4°N, 44.4°W), where the rates are strongly constrained by numerous data. Eurasia–North America stage rates are determined along the Reykjanes Ridge, where rates are similarly strongly constrained by abundant, unambiguous magnetic anomaly data. Dashed horizontal lines show the time intervals for which each stage rate is determined.

### 5.3 Simultaneous Nubia–North America and Eurasia–North America motion changes: geodynamic implications

The Nubia–North America stage spreading history during the Neogene is remarkably similar to that for the Eurasia–North America Plate boundary (Fig. 19) even though they are determined from independent data along two different plate boundaries. The 25 per cent slowdown in Nubia–North America spreading rates from 8.2 to 6.2 Ma coincides with a slowdown of comparable magnitude in Eurasia–North America spreading rates (Fig. 19). That plate motions along these two spreading-dominated plate boundaries change in tandem implies that their motions are coupled either via mantle convection that acts similarly along the bases of the two plates or via some combination of forces acting across their boundaries.

Iaffaldano *et al.* (2006) demonstrate that surface topography built at convergent margins can control the evolution of plate motion over millions of years by increasing the frictional forces between two converging plates. If the largely convergent Nubia–Eurasia Plate boundary strongly couples the movements of Nubia and Eurasia, then changes in the forces that act along either the Nubia–Eurasia Plate boundary or the boundaries of any of the Nubia, Eurasia or North America plates might result in simultaneous adjustments to the motions of all three plates. Better constraints on the Neogene kinematic history of Nubia–Eurasia motion would narrow the range of possible explanations, as would modelling of the kinematic responses of all three plates to plausible changes in the torques that have been driving their motions during the Neogene. In a forthcoming analysis, we undertake the former to test whether significant changes in Nubia–Eurasia motion have occurred during the Neogene.

### 5.4 Suitability for global plate circuit reconstructions

The new finite and plate motion rotations presented fill a key missing link in detailed reconstructions of global plate motions during the Neogene, as discussed by Molnar & Stock (2009). We are presently using the new reconstructions to link the motions of the plates in

the north Atlantic to plates in the Pacific and Indian Ocean basins. The new rotation estimates have considerable merits. Our implementation of Shaw & Cande's (1990) flow-line fitting function in our inversion procedure has resulted in a sequence of plate motion rotations that describe a smooth progression in the plate slip directions through time (Fig. 16B). This minimizes one source of noise that might propagate outwards into a global plate circuit. In addition, the scatter of the Chron 1n to 4A rotations is small and is generally consistent with the bootstrapped rotation uncertainties. The 2-D 95 per cent reconstruction uncertainties propagated from the covariances for Chrons 1n to 4A (Table 2) are typically  $\pm 1$  to 3 km, even for locations distant from the plate boundary. For comparison, the 2-D, 95 per cent reconstruction uncertainties for older reversals are as large as  $\pm 3$  to 6.5 km, reflecting the sparser coverage and higher likelihood of magnetic reversal misidentifications along some parts of the plate boundary.

Although the new rotations are a step forward from previous work, likely errors in our correlations of some older reversals along more sparsely parts of the plate boundary add undesirable noise to our rotation estimates. As this presumed noise propagates outwards into the global plate circuit, it will result in undesirable sudden changes in the motion estimates for other plate pairs unless some form of smoothing is applied. This calls for improved survey coverage of older reversals south of Kane FZ (24°N) and north of Atlantis FZ (30°N).

### ACKNOWLEDGEMENTS

We thank Joaquim Luis for providing us with magnetic data, and Steve Cande and Pete Shaw for software. We also thank Carmen Gaina and Saskia Goes for constructive comments and reviews. This work was supported by grant 06-05-64297 from the Russian Foundation for Basic Research and U.S. National Science Foundation grant OCE-0926274. Continuous GPS data were provided by (1) the Plate Boundary Observatory operated by UNAVCO and supported by National Science Foundation grants EAR-0350028 and EAR-0732947, (2) the Global GNSS Network operated by UNAVCO for NASA Jet Propulsion Laboratory under NSF Cooperative Agreement No. EAR-0735156, (3) the Scripps Orbit and Permanent Array Center and (4) the NOAA CORS archive. Figures were drafted using Generic Mapping Tools software (Wessel & Smith 1991).

### REFERENCES

- Altamimi, Z., Collilieux, X., Legrand, J., Garayt, B. & Boucher, C., 2007. ITRF2005: a new release of the International Terrestrial Reference Frame based on time series of station positions and Earth orientation parameters, *J. geophys. Res.*, **112**, B09401, doi:10.1029/2007JB004949.
- Altamimi, Z., Collilieux, X. & Metivier, L., 2011. ITRF2008: an improved solution of the international terrestrial reference frame, *J. Geodesy*, **8**, 457–473.
- Argus, D.F., 2007. Defining the translational velocity of the reference frame of Earth, *Geophys. J. Int.*, **169**, 830–838.
- Argus, D.F., Gordon, R.G., Heflin, M.B., Ma, C., Eanes, R., Willis, P., Peltier, W.R. & Owen, S.E., 2010. The angular velocities of the plates and the velocity of Earth's centre from space geodesy, *Geophys. J. Int.*, **180**(3), 913–960.
- Atwater, T. & Molnar, P., 1973. Relative motion of the Pacific and North American plates deduced from sea-floor spreading in the Atlantic, Indian, and South Pacific Oceans, in *Proceedings of the Conference on Tectonic Problems of the San Andreas Fault System*, Vol. 13, pp. 136–148, eds. Kovach, R.L. & Nur, A., Stanford Univ. Pub. Geol. Sci.

- Atwater, T. & Stock, J., 1998. Pacific-North America plate tectonics of the Neogene Southwestern United States: an update, *Int. Geol. Rev.*, **40**, 375–402.
- Calais, E., Han, J.Y., DeMets, C. & Nocquet, J.M., 2006. Deformation of the North American plate interior from a decade of continuous GPS measurements, *J. geophys. Res.*, **111**, B06402, 9–22.
- Cannat, M. *et al.*, 1999. Mid-Atlantic Ridge-Azores hotspot interactions: along-axis migration of a hotspot-derived event of enhanced magmatism 10 to 4 Ma ago, *Earth planet. Sci. Lett.*, **173**, 257–269.
- Carbotte, S.M. *et al.*, 2004. New integrated data management system for Ridge2000 and MARGINS research, *EOS, Trans. Am. geophys. Un.*, **85**, 553–559.
- Chang, T., 1988. Estimating the relative rotation of two tectonic plates from boundary crossings, *J. Am. Statist. Assoc.*, **83**, 1178–1183.
- Collette, B.J., Verhoef, J. & Roest, W.R., 1984. Geophysical investigations of the floor of the Atlantic Ocean between 10° and 38°N (Kroonvlag Project), Series B, *Proc. Koninklijke Nederlandse Akademie van Wetenschappen*, **87**, 1–76.
- DeMets, C. & Wilson, D.S., 2008. Toward a minimum change model for recent plate motions: calibrating seafloor spreading rates for outward displacement, *Geophys. J. Int.*, **174**, 825–841.
- DeMets, C., Gordon, R.G. & Argus, D.F., 2010. Geologically current plate motions, *Geophys. J. Int.*, **181**, 1–80.
- Detrick, R.S., Needham, H.D. & Renard, V., 1995. Gravity anomalies and crustal thickness variations along the Mid-Atlantic Ridge between 33°N and 40°N, *J. geophys. Res.*, **100**, 3767–3787.
- Fisher, N.I., Lewis, T. & Embleton, B.J.J., 1993. *Statistical Analysis of Spherical Data*, Cambridge Univ. Press, 329 pp.
- Fujiwara, T., Lin, J., Matsumoto, T., Kelemen, P.B., Tucholke, B.E. & Casey, J.F., 2003. Crustal evolution of the Mid-Atlantic Ridge near the Fifteen-Twenty fracture zone in the last 5 Ma, *Geochem. Geophys. Geosyst.*, **4**, doi:10.1029/2002GC000364.
- Gente, P. *et al.*, 1995. Characteristics and evolution of the segmentation of the Mid-Atlantic Ridge between 20°N and 24°N during the last 10 million years, *Earth planet. Sci. Lett.*, **129**, 55–71.
- Hellinger, S.J., 1979. The statistics of finite rotations in plate tectonics, *PhD thesis*, Massachusetts Institute of Technology, 172 pp.
- Hellinger, S.J., 1981. The uncertainties of finite rotations in plate tectonics, *J. geophys. Res.*, **86**, 9312–9318.
- Hilgen, F.J., Lourens, L.J. & Van Dam, J.A., 2012. The Neogene period, in *The Geologic Time Scale 2012*, pp. 947–1002, eds Gradstein, F.M., Ogg, J.G., Schmitz, M. & Ogg, G., Elsevier Science B. V.
- Iaffaldano, G., Bunge, H.-P. & Dixon, T.H., 2006. Feedback between mountain belt growth and plate convergence, *Geology*, **34**, 893–896.
- Kirkwood, B.H., Royer, J.-Y., Chang, T.C. & Gordon, R.G., 1999. Statistical tools for estimating and combining finite rotations and their uncertainties, *Geophys. J. Int.*, **137**, 408–428.
- Klitgord, D. K. & Schouten, H., 1986. Plate kinematics of the central Atlantic, in *The Western North Atlantic Region M*, pp. 351–378, eds Vogt, P.R. & Tucholke, B.E., The Geological Society of America.
- Kogan, M.G. & Steblov, G.M., 2008. Current global plate kinematics from GPS (1995–2007) with the plate-consistent reference frame, *J. geophys. Res.*, **113**, B04416, doi: 10.1029/2007JB005353.
- Lourens, L., Hilgen, F.J., Laskar, J., Shackleton, N.J. & Wilson, D., 2004. The Neogene period, in *A Geologic Time Scale 2004*, pp. 409–440, eds Gradstein, F., Ogg, J. & Smith, A., Cambridge Univ. Press.
- Macdonald, K.C., Miller, S.P., Luyendyk, B.P., Atwater, T.M. & Shure, L., 1983. Investigation of a Vine-Matthews magnetic lineation from a submersible: the source and character of marine magnetic anomalies, *J. geophys. Res.*, **88**, 3403–3418.
- Marquez-Azua, B. & DeMets, C., 2003. Crustal velocity field of Mexico from continuous GPS measurements, 1993 to June, 2001: implications for the neotectonics of Mexico, *J. geophys. Res.*, **108**(B9), doi: 10.1029/2002JB002241.
- Maschenkov, S. & Pogrebitysky, Y., 1992. Preliminary results of Canary-Bahamas Project, *EOS, Trans. Am. geophys. Un.*, **73**, 393–397.
- McQuarrie, N., Stock, J.M., Verdel, C. & Wernicke, B.P., 2003. Cenozoic evolution of Neotethys and implications for the causes of plate motions, *Geophys. Res. Lett.*, **30**(20), doi:10.1029/2003GL017992.
- Merkouriev, S. & DeMets, C., 2006. Constraints on Indian plate motion since 20 Ma from dense Russian magnetic data: implications for Indian plate dynamics, *Geochem. Geophys. Geosyst.*, **7**, Q02002, doi:10.1029/2005GC001079.
- Merkouriev, S. & DeMets, C., 2008. A high-resolution model for Eurasia-North America plate kinematics since 20 Ma, *Geophys. J. Int.*, **173**, 1064–1083.
- Molnar, P. & Stock, J.M., 2009. Slowing of India's convergence with Eurasia since 20 Ma and its implications for Tibetan mantle dynamics, *Tectonics*, **28**, TC3001, doi:10.1029/2008TC002271.
- Muller, R.D., Royer, J.-Y., Cande, S.C., Roest, W.R. & Maschenkov, S., 1999. New constraints on the Late Cretaceous/Tertiary plate tectonic evolution of the Caribbean, in *Caribbean Basins, Sedimentary Basins of the World*, Vol. 4, pp. 33–59, ed. Mann, P., Elsevier Science B. V.
- Roest, W.R. & Collette, B.J., 1986. The Fifteen-Twenty Fracture Zone and the North American-South American plate boundary, *J. Geol. Soc. Lond.*, **143**, 833–844.
- Roest, W.R., Arkani-Hamed, J. & Verhoef, J., 1992. The seafloor spreading rate dependence of the anomalous skewness of marine magnetic anomalies, *Geophys. J. Int.*, **109**, 653–669.
- Royer, J.-Y. & Chang, T., 1991. Evidence for relative motions between the Indian and Australian plates during the last 20 Myr from plate tectonic reconstructions: implications for the deformation of the Indo-Australian plate, *J. geophys. Res.*, **96**, 11 779–11 802.
- Sella, G.F., Dixon, T.H. & Mao, A., 2002. REVEL: a model for recent plate velocities from space geodesy, *J. geophys. Res.*, **107**(B4), doi:10.1029/2000JB000033.
- Sella, G.F., Stein, S., Dixon, T.H., Craymer, M., James, S., Mazzotti, S. & Dokka, R.K., 2007. Observation of glacial isostatic adjustment in 'stable' North America with GPS, *Geophys. Res. Lett.*, **34**(L02306), doi:10.1029/2006GL027081.
- Sempere, J.-C., Macdonald, K.C. & Miller, S.P., 1987. Detailed study of the Brunhes/Matuyama reversal boundary on the East Pacific Rise at 19°30' S: implications for crustal emplacement processes at an ultra fast spreading center, *Mar. Geophys. Res.*, **9**, 1–23.
- Shaw, P.R. & Cande, S.C., 1990. High-resolution inversion for South Atlantic plate kinematics using joint altimeter and magnetic anomaly data, *J. geophys. Res.*, **95**, 2625–2644.
- Sloan, H. & Patriat, P., 1992. Kinematics of the North American-African plate boundary between 28°N and 29°N during the last 10 Ma: evolution of the axial geometry and spreading rate and direction, *Earth planet. Sci. Lett.*, **113**, 323–341.
- Ward, S.N., 1990. Pacific-North America plate motions: new results from very long baseline interferometry, *J. geophys. Res.*, **95**, 21 965–21 981.
- Wessel, P. & Smith, W.H.F., 1991. Free software helps map and display data, *EOS, Trans. Am. geophys. Un.*, **72**, 441–446.
- Wilson, D.S., 1993. Confidence intervals for motion and deformation of the Juan de Fuca, *J. geophys. Res.*, **98**, 16 053–16 071.
- Wilson, D.S., McCrory, P.A. & Stanley, R.G., 2005. Implications of volcanism in coastal California for the Neogene deformation history of western North America, *Tectonics*, **24**, TC3008, doi:10.1029/2003TC001621.
- Zumberge, J.F., Heflin, M.B., Jefferson, D.C., Watkins, M.M. & Webb, F.H., 1997. Precise point positioning for the efficient and robust analysis of GPS data from large networks, *J. geophys. Res.*, **102**, 5005–5017.